Final Report

Project DE-EE0006761

SURFACE AND SUBSURFACE GEODESY COMBINED WITH ACTIVE BOREHOLE EXPERIMENTATION FOR THE ADVANCED CHARACTERIZATION OF EGS RESERVOIRS

Derek Elsworth, Kyungjae Im

Energy and Mineral Engineering

EMS Energy Institute

and

Center for Geomechanics, Geofluids and Geohazards

Pennsylvania State University

Yves Guglielmi[1] *and Glen Mattioli* [2]

[1]Lawrence Berkeley National Laboratory

[2]University of Texas Arlington and UNAVCO

November 14, 2016

SURFACE AND SUBSURFACE GEODESY COMBINED WITH ACTIVE BOREHOLE EXPERIMENTATION FOR THE ADVANCED CHARACTERIZATION OF EGS RESERVOIRS

Derek Elsworth, Kyungjae Im
Energy and Mineral Engineering, EMS Energy Institute and G3 Center, Pennsylvania State University
Yves Guglielmi[1] *and Glen Mattioli*[2]
[1]Lawrence Berkeley National Laboratory and [2]University of Texas Arlington and UNAVCO

Executive Summary

We explore the utility of combining active downhole experimentation with borehole and surface geodesy to determine both the characteristics and evolving state of EGS reservoirs during stimulation through production. The study is divided into two parts. We demonstrate the feasibility of determining *in situ* reservoir characteristics of reservoir size, strain and fracture permeability and their dependence on feedbacks of stress and temperature using surface and borehole geodetic measurements (**Part I**). We then define the opportunity to apply the unique hydraulic pulse protocol (HPP) borehole tool to evaluate reservoir state. This can be accomplished by monitoring and co-inverting measured reservoir characteristics (from the HPP tool) with surface geodetic measurements of deformation, tilt and strain with continuous measurements of borehole-wall strain (*via* optical fiber and fiber Bragg gratings) and measured flow rates (**Part II**).

Characterization and Monitoring of EGS Reservoirs: These studies have evaluated the potential for both direct and indirect measurement of permeability evolution, thermal depletion and the characterization of key parameters of EGS reservoirs. Apparent is that surface geodetic signals are indeed sufficiently large to monitor thermal contraction and fault reactivation and to estimate changes in the state of the reservoir. Signals anticipated from the HPP tool during radial injection into a fracture potentially provide key parameters for EGS reservoir development.

Surface deformation is a commonly observed phenomenon in various geothermal fields. This reflects subsurface volume change due to shrinkage and dilation or faulting and fault reactivation induced by fluid injection. Here we assess surface deformations (vertical displacement, surface tilt and horizontal strain) as signatures in two different modalities: (i) isotropic volume change (Mogi model) and (ii) injection induced shear offset (Okada slip model) and compare the results with the resolution of current geodetic tools. We assume a spherical fractured reservoir within an infinite medium and follow changes in the stress/strain field of the cooled inclusion. This behavior shows a tensional decoupling for a no-tension material that is induced as a result thermal destressing. This tensional decoupling is used to estimate the magnitude of the maximum detectable deformation recorded when thermal contraction ensues. Then the mechanism of permeability change induced by thermal contraction of the spherical inclusion (reservoir) is assessed. Comparison of predicted deformations with instrumental resolutions confirms that geodetic signals, especially tilt and strain, are indeed sufficiently large to describe reservoir evolution. Volume changes of the order of 10^3 m^3 (induced by thermal contraction during ~one month of geothermal

operation) or 1 mm of slip on a reactivated fault patch of 1000 m×500 m at a depth of 2500 m induce tilts of ~10 nano-radians and strains of ~10 nano-strains, which are ~10 times larger than the resolution of current near-surface geodetic instruments. Observed surface deformation together with field operation data in various geothermal projects suggest that both shear and normal displacement mechanisms contribute to the large deformations. Although the two different modes could induce surface deformation concurrently, we demonstrate that these modes can be identified through the temporal and spatial variation of surface deformation during individual sub-surface events.

In Situ Measurements with the Hot HPP Tool: The success of EGS requires both high-fluid-throughput and thermally-long-lived geothermal reservoirs. High-fluid-throughput in traditional basement rocks requires that reservoir permeabilities at depth (~5km) must be elevated from the microDarcy to the milliDarcy range and with long thermal life. A long-thermal life requires that high heat-transfer area is maintained concurrent with high flow rates. This is only feasible if fluid circulation in the reservoir has a broad and even sweep through media with a short thermal diffusion length (small fracture spacing) thus avoiding thermal short-circuiting and damaging feedbacks of thermal permeability enhancement. Therefore permeability control is a key requirement to develop a successful EGS reservoir. Thermally-driven permeability evolution results from induced strains around fractures that, in turn, result from temperature change. These deformations are strongly dependent on parameters of the fluid and rock such as thermal expansion coefficient, thermal conductivities, flow rate, fracture stiffness and *in situ* stress field. Measuring and analyzing the deformations together with permeability evolution *in situ* will describe fluid flow and conductive thermal energy transport in the reservoir and provide essential parameters to effectively develop EGS reservoirs. Such direct measurements of fracture deformation with permeability evolution have been successfully conducted with the unique hydraulic pulse protocol (HPP) probe (Guglielmi et. al. 2015 a&b). However, the current tool is limited to ~10 MPa and 80°C and not yet readily applicable to a high pressure high temperature environment. Here we explore the potential developments needed to elevate tool performance to 100 MPa and 300°C and necessary experimental protocols to maximize data recovered. In this work we examine (i) expected fracture deformation and recoverable HPP tool signals in an EGS system and (ii) a strategy to upgrade the current HPP tool to be stable in an HTHP environment. Deformations from cold water flow into a fracture and the expected HPP response of the tool are investigated by numerical simulations. These results indicate that there are two modalities of deformation: (i) immediate (<10 seconds) pressure-driven dilation of the fault/fracture and (ii) a second delayed thermally-induced response of opening and slip. Observed deformations are analyzed with the theory for a soft inclusion (Eshelby) and indicate that thermally-induced unloading and consequent deformations are strongly dependent on the hydro-thermal-mechanical properties of the reservoir and fracture. Stress evolution and its magnitude is determined by the morphology of the cooled volume. A flat cooling ellipsoid centered on the fracture results in thermal cracking (opening in the direction normal to the fracture) while fracture opening enlarges as cooling proceeds. We show that the stress field in the chilled inclusion can be approximated by the temperature change without considering the external thermal gradient. The analysis of cold water injection for one month (fracture zone of 4mm thickness and 10 Darcy permeability) resulted in ~3 mm of opening and

~6mm of slip. Expected HPP signals (deformations at ~30cm above the isolated fracture) are significantly larger than tool resolution confirming the utility of the tool to precisely measure the hydro-thermal-mechanical properties of the reservoir and to describe reservoir deformation behavior. Shear displacement signals are nearly identical to fracture surface deformation while normal displacement initially diverges from fracture opening reflecting thermal contraction of the reservoir between anchor and fracture surface.

Tool Design: We review current cold-HPP tool capabilities and required upgrades for deployment in geothermal systems. The current displacement measurement system (fiber Bragg grating) is fundamentally stable at HTHP conditions while the deformation cage and current packer system are not. The deformation cage itself may not require significant modification in design except the aluminum body and cage-fiber adhesive may need to be replaced by materials with a high durability to elevated temperature. Current neoprene packers will not survive and considerable modification in design is needed. Existing HTHP off-the-shelf packers are reviewed and requisite revisions to adopt the packer mechanism in the current HPP tool are discussed.

Journal Articles

Im, K.J., Elsworth, D., Guglielmi, Y. and Mattioli, G. (2016). Geodetic imaging of production, thermal depletion and fault reactivation in geothermal reservoirs. Submitted for publication. 40 pp.

Papers in Conference Proceedings

Im, K.J., Elsworth, D. (2015). Use of Geodesy to Discriminate the Deformation Mechanics in Geothermal Reservoir. Proceedings 49th US Rock Mechanics and Geomechanics Symposium. 28 June ~ 1 July

SURFACE AND SUBSURFACE GEODESY COMBINED WITH ACTIVE BOREHOLE EXPERIMENTATION FOR THE ADVANCED CHARACTERIZATION OF EGS RESERVOIR

Derek Elsworth, Kyungjae Im
Energy and Mineral Engineering, EMS Energy Institute and G3 Center, Pennsylvania State University
Yves Guglielmi[1] and Glen Mattioli[2]
[1]Lawrence Berkeley National Laboratory and [2]University of Texas Arlington

Table of Contents

PART I: GEODETIC IMAGING OF PRODUCTION THERMAL DEPLETION AND FAULT REACTIVATION IN GEOTHERMAL RESERVOIRS

PART II: HOT HPP TOOL: CHARACTERIZING THE EVOLUTION OF STRESS AND PERMEABILITY AND ENGINEERING DESIGN

PART I: GEODETIC IMAGING OF PRODUCTION THERMAL DEPLETION AND FAULT REACTIVATION IN GEOTHERMAL RESERVOIRS

Derek Elsworth, Kyungjae Im
Energy and Mineral Engineering, EMS Energy Institute and G3 Center, Pennsylvania State University
Yves Guglielmi[1] and Glen Mattioli[2]
[1]Lawrence Berkeley National Laboratory and [2]University of Texas Arlington

Table of Contents

Abstract

Surface deformation is a commonly observed phenomenon in various geothermal fields. This reflects subsurface volume change due to shrinkage and dilation or faulting and fault reactivation induced by fluid injection. Here we assess surface deformations (vertical displacement, surface tilt and horizontal strain) as signatures in two different modalities: (i) isotropic volume change (Mogi model) and (ii) injection induced shear offset (Okada slip model) and compare the results with the resolution of current geodetic tools. We assume a spherical fractured reservoir within an infinite medium and follow changes in the stress/strain field of the cooled inclusion. This behavior shows a tensional decoupling for a no-tension material that is induced as a result thermal destressing. This tensional decoupling is used to estimate the magnitude of the maximum detectable deformation recorded when thermal contraction ensues. Then the mechanism of permeability change induced by thermal contraction of the spherical inclusion (reservoir) is assessed. Comparison of predicted deformations with instrumental resolutions confirms that geodetic signals, especially tilt and strain, are indeed sufficiently large to describe reservoir evolution. Volume changes of the order of 10^3 m^3 (induced by thermal contraction during ~one month of geothermal operation) or 1 mm of slip on a reactivated fault patch of 1000 m×500 m at a depth of 2500 m induce tilts of ~10 nano-radians and strains of ~10 nano-strains, which are ~10 times larger than the resolution of current near-surface geodetic instruments. Observed surface deformation together with field operation data in various geothermal projects suggest that both shear and normal displacement mechanisms contribute to the large deformations. Although the two different modes could induce surface deformation concurrently, we demonstrate that these modes can be identified through the temporal and spatial variation of surface deformation during individual sub-surface events.

1. Introduction

Surface deformations of significant magnitude in a number of geothermal fields have been observed by both interferometric methods (InSAR) (Ali et al, 2016, Eneva et al 2012, Falorni et al 2011, Fialko and Simons 2000, Foxall and Vasco 2003, Vasco et al 2002, Vasco 2013) and by direct measurement of surface tilt (Vasco et al 2002). Subsurface deformations induced by cold water injection generally conform to two different modalities: (i) isotropic volume change and (ii) injection induced shear offset on finite faults. Isotropic volume change can be induced by either thermal contraction (volume decrease) or pressure dilation (volume increase) in the reservoir with shear slip similarly resulting from changes in effective stress induced by changes in fluid pressures or temperature. Ali et. al. (2016) recently show that surface subsidence in the Brady Hot Springs geothermal field may result from the contraction of shallow strata similar to the potential for pressure driven early-time slip and temperature driven late-time slip postulated to result in geothermal reservoirs (Gan and Elsworth, 2014).

Although surface deformation can be induced by both pressure and temperature change. However, observations suggest that these deformations may be mainly temperature driven since they are both slow and continuous. Surface subsidence rates are typically several cm/year and continue throughout geothermal operations. As discussed by Gan and Elsworth (2014), temperature driven stress change is slow and continues until the reservoir is thermally depleted. Conversely, pressure change is concentrated at early time injection, limited by boundaries (well bore pressures) and typically localized near-wellbore regions of injection or production, where effects are most focused.

Linking the observed deformation with a subsurface mechanism helps define active processes during reservoir evolution. Such models may be used to constrain magnitudes of thermal energy transfer from rock to fluid, fluid leakage, and the evolution of transport characteristics of the reservoir. The detection of slip processes on finite faults in turn constrains fluid flow and the evolution of major flow paths, and may allow the precursors to injection-induced seismicity to be defined and monitored.

There is a significant loss of information when a 3D subsurface deformation field is projected onto a 2D surface. This degradation in information may be stemmed if additional independent, but mechanistically-linked observations are made. For example, volume change can be estimated by measuring both net fluid loss and net thermal volume change and this may be compared with the measured thermal budget of the reservoir. In addition, micro-seismicity data also are useful in constraining slip processes, either as a single event (hypocentral location, magnitude, and where available, focal mechanisms) or as stacked data that would yield an equivalent net shear displacement – the ensemble due to multiple events.

Below, we assess the potential to use surface and subsurface geodetic measurements to interpret hydrothermal reservoir processes. We examine the expected magnitudes of displacement, tilt and strain resulting for production from geothermal reservoirs and compare this with the instrumental resolution of common measurements. We use the Mogi volumetric model (Mogi 1958) and the Okada shear slip model (Okada 1985) within an elastic half-space to define signal magnitudes with consideration of coupling and decoupling process between reservoir and surrounding rock. We then compare these results with the resolution of current geodetic methods. Finally, we analyze existing surface deformation data using these models to deconvolve processes within deep reservoirs.

2. Surface Deformation

We assess surface deformation developed by two modes of subsurface displacement: (i) volume change due to thermal contraction and (ii) shear deformation due to slip on a finite fault plane. We apply the Mogi (1958) solution to analyze volume change and the Okada (1985) solution for shear deformation offset at depth to estimate the magnitude of maximum deformations: vertical displacement, surface tilt and strain.

2.1 Volume Change

Volumetric strain, ε_v, induced by temperature change in an unconstrained medium is

$$\varepsilon_v = \alpha_v \Delta T \tag{1}$$

where, α_v is volumetric thermal expansion coefficient and ΔT is temperature change. Experimental data indicate that the volumetric thermal expansion coefficient of igneous rock is generally within the range 2×10^{-5}~7×10^{-5} within the temperature range between 30°C and 400°C (Cooper and Simmons 1977). The magnitude of the thermal expansion coefficient suggests that thermal stresses can surpass poroelastic stresses in typical geothermal systems after sufficient duration of injection/recovery. For example, a temperature change of 150°C with $\alpha_v=3\times10^{-5}$ induces a volumetric strain of 0.0045 while a 20 MPa change in pressure with a bulk modulus of 20 GPa induces a volumetric strain of only 0.001 in an unconfined system.

2.1.1 Coupled Deformation

Eqn. (1) assumes a change in strain with not net change in stress. The presence of the surrounding rock, however, reduces the magnitude of deformation (Eshelby, 1957). To estimate this effect on the resulting volumetric strain arising from thermal expansion, we analyze a spherical fractured reservoir that has a modulus different from that of the surrounding rock (spherical soft inclusion). The Young’s modulus of the fractured reservoir can be expressed as (Goodman, 1980),

$$\frac{1}{E_{res}} = \frac{1}{E} + \frac{1}{k_n S} \tag{2}$$

where, k_n is normal stiffness of an individual fracture and S is fracture spacing and E is the Young's modulus of the intact rock. Accordingly, the fractured rock will generally be less stiff than the intact rock.

Fig. 1 illustrates deformations due to a change in pressure within (i) a spherical reservoir under zero stress, (ii) a spherical cavity in an infinite medium and (iii) their coupled behavior. The magnitude of the coupled strain can be recovered as follows. Volumetric strain induced by pressure change in the unconstrained spherical reservoir of bulk modulus K_{res} (**Fig. 1 (a)**) is

$$\varepsilon_{v,sphere} = \frac{\Delta P_{sphere}}{K_{res}} \tag{3}$$

Volumetric strain induced by pressure change in the spherical cavity in an infinite body (host rock) with shear modulus G_{host} (**Fig. 1 (b)**) is

$$\varepsilon_{v,cavity} = \frac{\Delta P_{cavity}}{\frac{4G_{host}}{3}} \tag{4}$$

If the sphere is embedded in the cavity and both sphere and cavity deform together with the same pressure change in the sphere, then the deformation of both sphere and cavity will be the same, with the same volumetric strain (boundary displacements linked), as,

$$\varepsilon_v = \varepsilon_{v,sphere} = \varepsilon_{v,cavity} \tag{5}$$

and the total pressure change used to deform both sphere and cavity is the sum of the applied pressures that induce the strain in both sphere and cavity,

$$\Delta P = \Delta P_{sphere} + \Delta P_{cavity} \tag{6}$$

Eqn. (3), (4), (5) and (6) yield volumetric strain of coupled deformation as (**Fig. 1 (c)**),

$$\varepsilon_v = \frac{\Delta P}{K_{res} + \frac{4G_{host}}{3}} \tag{7}$$

The equivalent pressure due to the thermal stress can be calculated by equating Eqn. (1) and (3),

$$\Delta P = K_{res} \alpha_v \Delta T \tag{8}$$

Substituting Eq. (8) into (7) yields

$$\varepsilon_v = \frac{1}{1+\frac{4G_{host}}{3K_{res}}}\alpha_v \Delta T \tag{9}$$

or,

$$\varepsilon_v = \frac{1}{1+\frac{2(1-2\nu)}{(1+\nu)}\frac{E_{host}}{E_{res}}}\alpha_v \Delta T \tag{10}$$

where, ν is Poisson's ratio and E_{host} and E_{res} are the Young's modulus of the host rock and reservoir rock, respectively. Note that the result is identical to that of an Eshelby spherical inclusion when $E_{host}=E_{res}$. Although this work focuses on a spherical cooled (mature) reservoir, the correspondence between Eqn (10) and that for an Eshelby inclusion indicates that the solution can be extended to an arbitrarily shaped ellipsoid.

Eqn. (10) indicates that the change in stress/strain inside a uniformly cooled sphere in an infinite medium is also uniform and this is independent of the form of the external temperature field. Imagine a sphere that is cooled by ΔT and sustains a volumetric strain of ε_v. If a concentric inner sphere inside this outer sphere is cooled by an additional ΔT then Eqn (10) (and the Eshelby solution) defines the induced strain in the inner sphere simply as $2\varepsilon_v$, which is identical to the case of a single sphere cooled by $2\Delta T$ without outer sphere. This result reveals that the existence of an outer sphere does not affect the stress/strain field of an embedded inner sphere. Thus thermal gradient in the outer shell does not affect the stress/strain field inside the embedded cooled sphere if the moduli are independent of temperature and the thermal gradient is also radially symmetric This observation significantly simplifies the stress/strain field and the resulting evaluation of permeability evolution.

Since $\alpha_v\Delta T$ is the unconstrained volumetric strain (Eqn (1)), the multipliers on $\alpha_v\Delta T$ in Eqn. (9) and (10) indicate the ratio of deformation reduction due to the existence of the surrounding rock. Since the elastic modulus of the fractured rock is generally smaller than that for unfractured rock (Eqn. (2)), the reduction ratio is maximum when $E_{host}=E_{res}$. For example, when $E_{host}=E_{res}$ and Poisson's ratio 0.25, the deformation ratio is 0.56. That is, the constrained volumetric strain magnitude arising from thermal expansion (or contraction) would be reduced to 56% of the zero stress case.

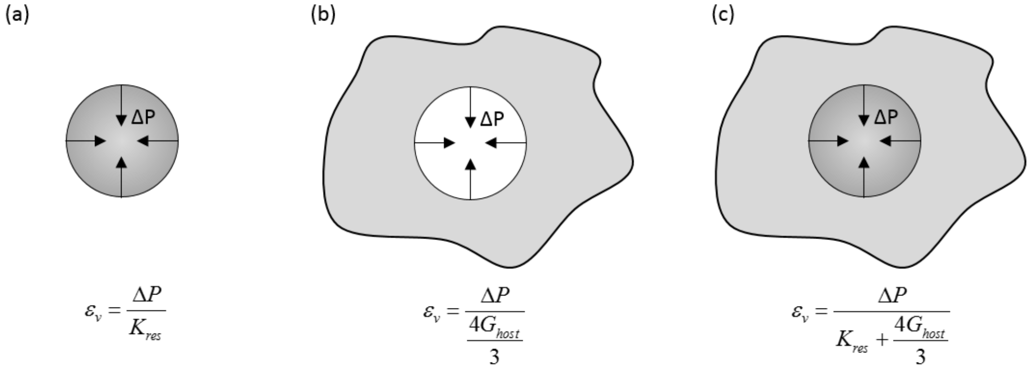

Figure 1. Volumetric strain induced by pressure change, *ΔP*, of (a) zero stress (no surroundings) sphere with bulk modulus K_{res}, and, (b) spherical cavity in an infinite body with shear modulus G_{host}. When the sphere and cavity deform with the same volumetric strain, the volumetric modulus of the coupled deformation (c) becomes the sum of bulk modulus of (a) and (b), $K_{res}+4G_{host}/3$.

2.1.2 Decoupling Between Reservoir and Host

The reduction of thermal contraction rate in coupled deformation (difference between Eqn (1) and Eqn (9)) indicates that the stress that resists thermal contraction would be induced in the reservoir. Thermal contraction will reduce the applied *in situ* stress in the reservoir and may eventually induce extensional stress. When the net stress of the reservoir becomes extensional and if the reservoir is highly fractured, further thermal contraction would open internal existing fractures rather than pulling-in the surrounding rock. Accordingly, the deformation of the reservoir and the surrounding rock decouples and Eqn. (5) is no longer valid.

A simple, idealized case for the decoupling of a spherical reservoir is analyzed here. Imagine an infinite elastic body with isotropic far field stress σ. If we remove a sphere from the body, then the stress change at the spherical cavity surface is $-\sigma$ and therefore the volumetric strain at the boundary of cavity with the infinite body is (Eqn. (4))

$$\varepsilon_{v,host} = -\frac{3\sigma}{4G_{host}} \tag{11}$$

If the spherical reservoir, which was removed from the infinite elastic body, is then placed in a stress free environment and cooled by ΔT, it would initially undergo expansion due to its removal from the infinite body with a strain equal to $\varepsilon_v=\sigma/K$, and simultaneously would contract due to the temperature change with strain equal to $\varepsilon_v=\alpha_v\Delta T$. The total volumetric strain on the spherical reservoir is then given by,

$$\varepsilon_{v,res} = \frac{\sigma}{K_{res}} + \alpha_v \Delta T \tag{12}$$

Fig. 2 illustrates the volumetric strains of (a) a stress-free cavity, (b) a stress-free spherical reservoir and (c) their coupled deformation. When an insulated spherical reservoir cools in an infinite body, the volumetric strain induced by the temperature change of the reservoir is governed by Eqn. (9) (coupled deformation, **Fig.2 (c)**). Once the magnitude of the induced volumetric strain becomes greater than the strain of the stress-relieved cavity (Eqn. (11)), however, further coupled deformation would induce extensional stresses on both reservoir and cavity wall. Assuming a no-tension criterion on the boundary of the reservoir and the cavity wall, the deformation decouples and may be separated into the distinct deformations of a stress-free cavity (**Fig. 2 (a))** and a stress-free sphere (**Fig. 2 (b)**).

As illustrated in **Fig 2 (d)**, all three volumetric strain curves (stress free cavity (a), stress free sphere (b) and coupled deformation (c)) coincide at a single decoupling point. Therefore the decoupling point can be calculated by equating any two of the equations (9), (11) and (12). The volumetric thermal stress at the decoupling point is,

$$K_{res}\alpha_v \Delta T = -\left(\frac{3K_{res}}{4G_{host}} + 1\right)\sigma \tag{13}$$

Rearranging Eqn. (13), we obtain the temperature drop to induce decoupling as

$$\Delta T_{decouple} = -\left(\frac{3K_{res}}{4G_{host}} + 1\right)\frac{\sigma}{K_{res}\alpha_v} \tag{14}$$

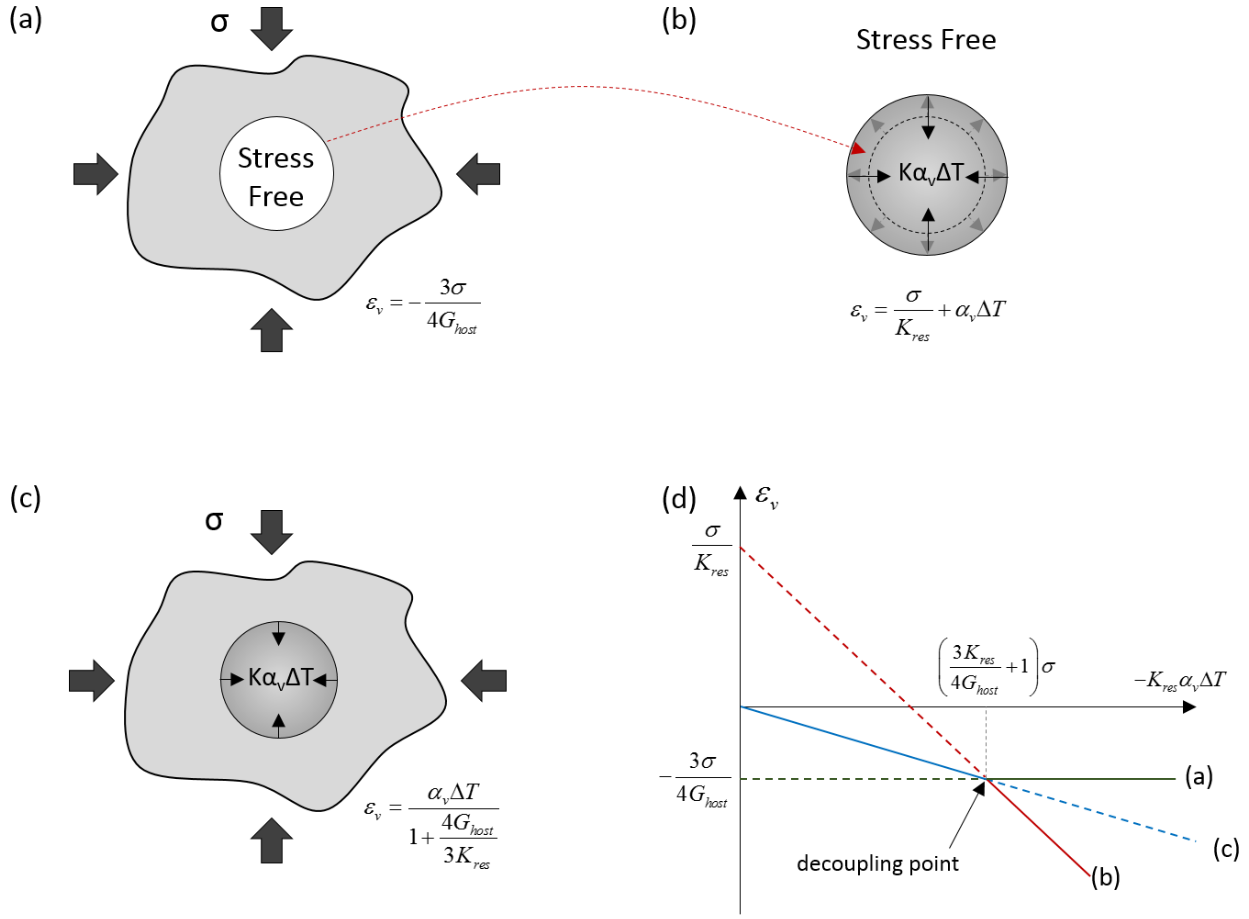

Figure 2. Spherical coupled and decoupled deformations in an infinite body with isotropic far field stress. When a spherical reservoir is removed from a body subjected to an isotropic far field stress σ and the remainder of the cavity is stress free, (a) there will be constant volumetric strain applied to the cavity as $-3\sigma/4G_{host}$. If the excluded spherical body is placed in a stress free environment and cooled with a temperature difference ΔT, the sphere will have a volumetric strain σ/K_{res} (expansion due to stress removal) plus $\alpha_v\Delta T$ (thermal expansion/contraction). Case (c) represents the coupled deformation as described in Eqn. (9). A volumetric strain vs. thermal stress ($-K_{res}\alpha_v\Delta T$) for all of cases ((a), (b) and (c)) is plotted in (d). The graph shows that all 3 cases intersect at one decoupling point. During the initial stage of falling temperature for a sphere in an infinite body (c), the volumetric strain is defined by coupled deformation (blue solid line); then after the decoupling point, the cavity (a) and the reservoir (b) will be decoupled into two stress free deformations (green solid line for the surrounding rock and the solid red line for the spherical reservoir).

Eqn. (14) defines the magnitude of temperature drop that induces tensional stress in the reservoir. If the reservoir is highly fractured, any further temperature drop will result in opening of the fractures rather than extending the surrounding rocks and the deformation of the rock surrounding the cavity will be significantly reduced – this will result in decreased deformation signal at the surface. The decoupling temperature versus isotropic far field stress is plotted for various bulk moduli in **Fig. 3** (assuming $E_{res} = E_{host}$, $\nu = 0.25$ and $\alpha_v = 5\times10^{-5}$). The plot shows the maximum absolute temperature difference for coupled deformation and, as a result, produces the maximum detectable surface deformation. For example, if K_{res} = 20 GPa and the isotropic far field stress is 50 MPa, then the maximum surface deformation would occur when the reservoir rock is cooled to ~110°C. Accordingly, if the rock is cooled by >110°C, the measured surface deformation signal will be limited to the threshold temperature change.

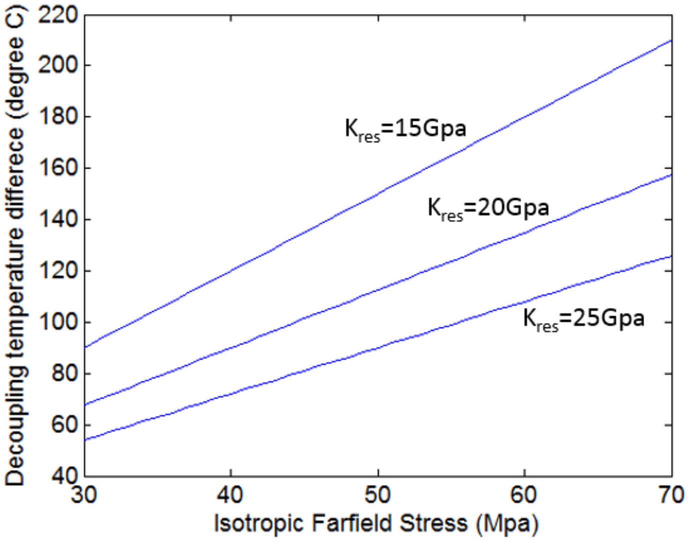

Figure 3. Decoupling temperature vs. isotropic far field stress with various reservoir bulk moduli. The plot assumes E_{res}=E_{host}, ν=0.25 and α_v=5×10^{-5}. The decoupling temperature difference represents the maximum temperature change that can be detected on the surface. For example, in the case of a far field stress of 50 MPa with K_{res} 20 GPa, ΔT~110°C induces a maximum surface deformation and further cooling will induce little (or no) additional surface deformation.

2.1.3 Permeability Change from Spherical Cooling

It has been shown that the stress applied within the reservoir decreases with thermal contraction and may eventually reach zero (**Fig. 2**). Thus, such thermal contraction would be expected to result in a concomitant increase in permeability. The following assesses this permeability change using a simple model of isotropic coupled deformation induced by uniform cooling within an embedded spherical reservoir.

The mechanism that induces volume change due to coupled thermo-mechanical unloading (Eqn. (9)) may be divided into two different modalities: (i) thermal contraction (assuming constant stress) and (ii) expansion due to stress decrease. Although such mechanisms act concurrently, considering them separately allows us to examine each of the processes and to calculate the magnitude of each effect in terms of the permeability change. We consider a spherical reservoir with equally spaced orthogonal fractures as illustrated in **Fig. 4**, showing (a) initial state of the reservoir, (b) thermal contraction under constant stress and (c) expansion due to stress decrease. Note that the temperature decrease (Fig. 4. (a) transitioning to (b)) would contract both rock matrix and pore space together. In contrast, in the process of stress reduction (Fig. 4. (b) transitioning to (c)), the modulus difference between rock matrix and fracture leads to an unbalanced expansion of the rock matrix and fracture.

The permeability of a rock with a set of parallel fractures with aperture *b* and spacing *S* can be defined as

$$k = \frac{b^3}{12S} \tag{15}$$

We assume that the fracture is held open by rock bridges of height, b, that contract with a change in temperature. Induced strain on both fracture and rock matrix due to the temperature change ΔT with volumetric thermal expansion coefficient α_v in constant stress (Fig. 4 (a) transitioning to (b)) are simply ($\alpha_v \Delta T$)/3. So aperture changes as $b(1+(\alpha_v \Delta T)/3)$ and fracture spacing changes to $S(1+(\alpha_v \Delta T)/3)$. Substituting the result into Eqn (15) yields the permeability due to thermal contraction at constant stress as

$$k_{thermal} = \frac{b^3}{12S}\left(1+\frac{\alpha_v \Delta T}{3}\right)^2 \tag{16}$$

Permeability decreases only slightly with temperature drop since $(\alpha_v \Delta T)/3$ is typically of the order of 10^{-3}, the permeability change is not significant.

The second influence is the change in stress that acts within the reservoir. Due to the difference in modulus between fracture and rock matrix, the fracture is strained more than the rock matrix, with this conditioned by the difference in effective modulus of the fracture versus the matrix. This may result in a significant permeability increase (Fig. 4 (b) transitioning to (c)). A relationship between permeability and strain (as a result of stress change) defines the change in permeability with normal (linear) strain change $\Delta \varepsilon_l$ as modulated by aperture, fracture spacing and modulus reduction ratio R_e (Ouyang and Elsworth, 1993; Liu et al 2000) as

$$k_{strain} = \frac{b^3}{12S}\left\{1+\left[\frac{S}{b}(1-R_e)+1\right]\Delta \varepsilon_l\right\}^3 \tag{17}$$

The modulus reduction ratio R_e is defined as

$$R_e = \frac{E_m}{E} \tag{18}$$

where E and E_m are modulus of intact rock and rock mass modulus respectively.

The total volumetric strain induced by thermal contraction within the surrounding rock is derived as Eqn (9). Therefore the strain change due to stress reduction (Fig 4 (b) transitioning to (c)) is the difference between the total strain (Eqn (9)) and thermal contraction in constant stress ($\alpha_v \Delta T$), which is,

$$\Delta \varepsilon_v = -\frac{\alpha_v \Delta T}{1+\frac{3K_{res}}{4G_{host}}} \tag{19}$$

Substituting Eqn. (19) into Eqn (17) and assuming isotropic conditions $\Delta\varepsilon_l=\Delta\varepsilon_v/3$, we recover the permeability as

$$k_{strain}=\frac{b^3}{12S}\left\{1+\left[\frac{S}{b}(1-R_e)+1\right]\frac{-\alpha_v\Delta T}{3\left(1+\frac{3K_{res}}{4G_{host}}\right)}\right\}^3 \tag{20}$$

Note that $b^3/12S$ is the original permeability, therefore the parameter in the brackets in Eqn. (20) represents the ratio of permeability increase. The permeability increases with a decrease in temperature and its magnitude may be significant, depending on the magnitudes of S/b and R_e.

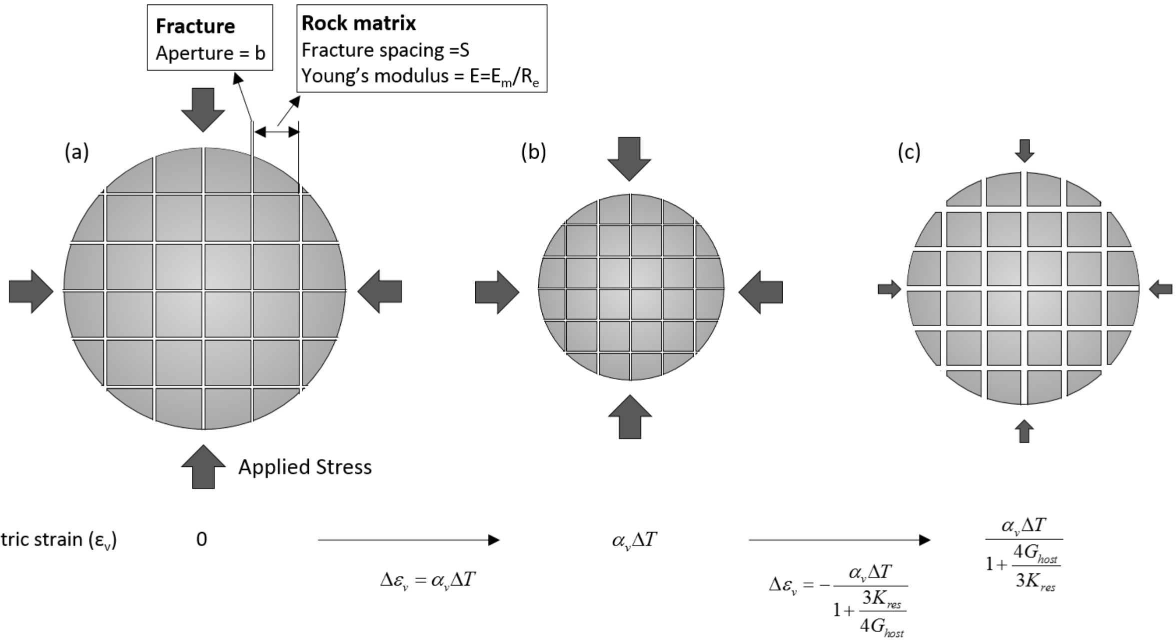

Figure 4. Schematic illustration of two mechanisms of volume change due to coupled thermal contraction: (i) thermal contraction (ii) stress reduction. Thermal contraction at constant stress will decrease both aperture and fracture spacing but strain driven by the concomitant reduction in stress results in a net increase in permeability.

Once quenching of the reservoir results in zero stress within the reservoir (reservoir stress decoupling) then further cooling results in an even larger rate of permeability increase with temperature drop. Assuming the boundary between the external host and the reservoir is stationary, aperture increase would be identical to the liner thermal contraction of rock matrix. That gives,

$$\Delta b=-\Delta S=-S\frac{\alpha_v\Delta T}{3} \tag{21}$$

Using this aperture change and ignoring any change in fracture spacing (due to thermal contraction of the blocks of the order of $\Delta S \sim S\alpha_l \Delta T$), permeability will become

$$k = k_d \left(1 - \frac{S}{b_d}\frac{\alpha_v \Delta T_d}{3}\right)^3 \tag{22}$$

where, k_d and b_d is the permeability and aperture at the temperature of decoupling and ΔT_d is temperature change from the decoupling point.

2.1.4 Surface Deformation from Geothermal Operations

The Mogi expressions (Mogi, 1958) for an isotropic spherical pressure source in an elastic half space defines vertical displacement due to subsurface volume change ΔV as,

$$u_v(r) = \frac{3}{4\pi}\frac{z}{R^3}\Delta V \tag{23}$$

where, z is depth of the source, and $R^2 = r^2 + z^2$ where r is horizontal (*i.e.* radial) distance from the source center. The surface tilt, θ, and surface radial strain, ε_r, arising from a Mogi source are defined as,

$$\theta(r) = -\frac{9}{4\pi}\frac{rz}{R^5}\Delta V \tag{24}$$

and

$$\varepsilon_r = \frac{3}{4\pi}\frac{1}{R^3}(1 - \frac{3r^2}{R^2})\Delta V \tag{25}$$

Thermal contraction rate induced by heat transfer from the rock to the fluid in a geothermal field is indexed by the heat extraction rate. Assuming a constant fluid flow rate Q_f with constant temperature difference between injection and production ΔT_f, the rate of heat energy gain of the injected fluid in the reservoir can be expressed as,

$$\dot{H}_f = Q_f \rho_f C_f \Delta T_f \tag{26}$$

Similarly, the heat energy loss from the rock is,

$$\dot{H}_r = V_r \rho_r C_r \dot{T}_r \tag{27}$$

where, ρ_f and ρ_r are density of fluid and rock, C_f and C_r are heat capacity of the fluid and rock respectively, V_r is the volume of rock and $\dot{T}_r$ is the rate of temperature change of the rock.

Equating Eqn. (26) and Eqn. (27) yields the expression for the rate of temperature change in the reservoir rock as,

$$\dot{T}_r = \frac{Q_f}{V_r}\frac{\rho_f C_f}{\rho_r C_r}\Delta T_f \tag{28}$$

Assuming a spherical reservoir, the constrained volumetric strain rate can be recovered by substituting Eqn. (28) into Eqn. (10).

$$\varepsilon_v = \frac{\dot{V}_r}{V_r} = \frac{1}{1+\frac{2(1-2\nu)}{(1+\nu)}\frac{E_{host}}{E_{res}}}\alpha_v \frac{1}{V_r}\frac{\rho_f C_f}{\rho_r C_r} Q_f \Delta T_f \tag{29}$$

Finally, multiplying by rock volume V_r in Eqn. (27), subsurface volume change rate can be recovered as

$$\dot{V}_r = \frac{1}{1+\frac{2(1-2\nu)}{(1+\nu)}\frac{E_{host}}{E_{res}}}\alpha_v \frac{\rho_f C_f}{\rho_r C_r} Q_f \Delta T_f \tag{30}$$

Substituting Eqn. (30) into the Mogi expression (Eqn. (23), (24) and (25)), we can obtain surface deformation rates induced by thermal contraction. Note Eqn. (30) is a maximum estimation since the decoupling process is not considered.

Expected maximum surface deformation after 1 year of operation of an geothermal field, assuming Q_f=0.1m^3/s, α=5×10^{-5}/K, $(\rho_f C_f)/(\rho_r C_r)$=2, $E_{host}=E_{res}$ and Poisson's ratio 0.25 with various geothermal gradients, is presented in **Fig. 5**. ΔT_f is calculated from the geothermal gradient assuming that temperature of the injection fluid and production fluid are identical to ground surface temperature and reservoir temperature, respectively. Deeper source depths yield higher reservoir temperatures and result in a larger volume change. Under these assumptions, the results indicate that the resolutions of current geodetic tools for tilt and strain (~1 nano-radian and ~1 nano-strain, respectively) are generally resolvable for any given source depth, while vertical displacement is not (~1 mm).

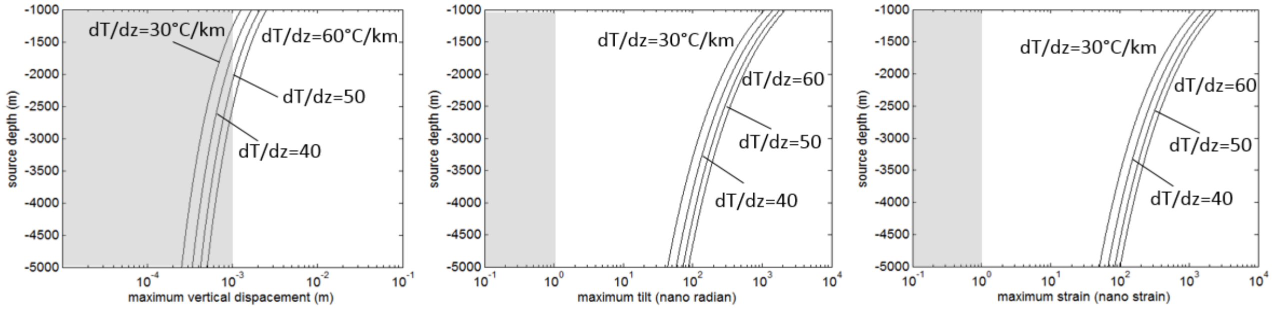

Figure 5. Maximum surface deformations *vs.* source depth with various geothermal gradients. (a) Vertical displacement, (b) surface tilt and (c) radial strain. Assumed parameters are, Q_f=0.1m^3/s, α=5×10^{-5}/K, E_{res}=E_{host}, Poisson's ratio 0.25 and 1 year of thermal production. Vertical displacement for a reservoir deeper than 1000 m is marginally resolvable with current geodetic tool resolution (~1 mm), while tilt and strain for all reservoir depths and for all geothermal gradients are larger than current geodetic tool resolutions (at ~1 nanoradian and ~1 nanostrain, respectively). Gray area in the panels denotes undetectable deformation.

A simple one-dimensional model describing thermal drawdown and consequent volume change patterns in geothermal reservoirs is explored in **Fig. 6**. The model compares two end-members of thermal drawdown behavior: (i) the case where a sharp thermal front transits the reservoir (**Fig. 6**. (a) red) and (ii) the case where uniform thermal drawdown occurs (*i.e.*, thermal front absent case, **Fig. 6**. (a) blue). Where the thermal front is present, heat flow from the rock to the fluid is sufficiently rapid that the temperature of the reservoir is partitioned between cold (thermally depleted) and hot zones. Conversely, where the thermal front is absent, temperature in the reservoir is uniform, as are the thermal strains.

The model describes a reservoir 1000 m × 200 m × 200 m at a depth of 2500 m with reservoir properties of volumetric thermal expansion coefficient α=5×10^{-5}, E_{res}=E_{host} and Poisson's ratio 0.25. Cold water (ΔT=-100ºC) is injected at one end of the reservoir and produced at the other. The reservoir is divided into 10 equal-sized zones with equivalent Mogi sources located at the center of each. The resulting surface deformation is determined by the activated superposed Mogi solutions from each source. Where the thermal front is present, the temperature decreases by 100ºC only at selected zones near the injector. For the uniform thermal depletion model, the temperature change and resulting strain is distributed uniformly between all zones. (**Fig. 6 (a)**).

The resulting surface deformation signals of vertical displacement, tilt and strain with three different depletion states (10 %, 30 % and 50 % depleted) are shown in **Fig. 6**. The red curves denote the case for the sharp thermal front and blue curves denote the case of uniform depletion with maximum, minimum and zero values marked by circles. The maximum, minimum and zero values migrate for the thermal front but are stationary for uniform depletion. **Fig 6** (e), (f) and (g) represent the differences in deformation magnitudes at the injection point (-500 m), the middle of the reservoir (0 m) and at the production location (500 m) for the contrasting cases of plug- and uniform-depletion. The two end member responses to depletion can be clearly identified by the magnitude of tilt (maximum difference ~230 nano-radians) and strain (maximum difference ~110 nano-strains) although not with vertical displacement (maximum difference ~0.1mm). This simple model shows that the magnitude of surface deformation, and its variation, is sufficient to identify the reservoir depletion behavior and therefore specific geodetic tools could be used for reservoir imaging of thermal depletion.

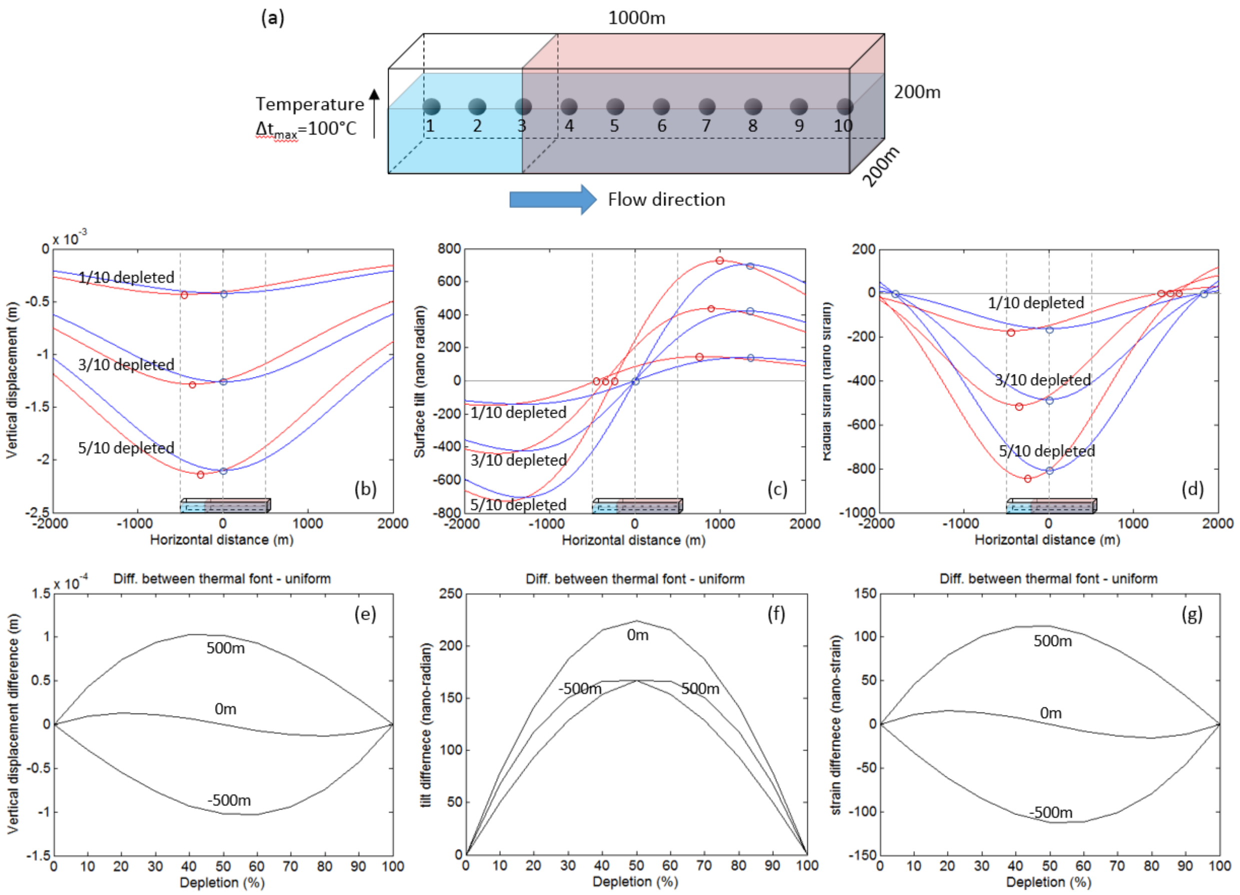

Figure 6. Surface geodetic signals of thermal front present (red) and absent (blue) case. 1000 m × 200 m × 200 m size reservoir is placed at a depth of 2500 m. The reservoir is divided by 10 equal sized zone with Mogi source at the center of each zone. Surface deformations are calculated by superposed Mogi solutions assuming α_v=5×10^{-5}, ΔT=100°C, $E_{res}=E_{host}$ and Poisson's ratio 0.25 (Eqn. (10)). Plots (b), (c) and (d) represent the geodetic signals on the surface and plots (e), (f) and (g) represent the difference of geodetic signals between thermal front present and absent cases at certain surface locations (injection point, middle of the reservoir and production point). It is clear that the difference in the thermal drawdown behavior can be identified with currently available tilt and strain meters but not with standard tools that can measure vertical displacement (*e.g.* GPS and InSAR). For uniform drawdown, the deformation profile is fixed in space but only changes in magnitude. For the moving thermal front, the center of the moves with the thermal front as in plots (b), (c) and (d). Since the gradient of tilt is maximum near the zero tilt point (plot (c)), any tilt observation has good spatial resolution near the point of zero tilt.

2.2 Shear Deformation

A number of seismic events, some of significant magnitude (M>3), occur simultaneous with fluid circulation in geothermal reservoirs (Majer et. al, 2007). Monitoring the shear offset of such faulting using surface or near-surface geodetic tools could potentially allow the visualization of the evolving major flow paths within the geothermal reservoir, and thus an analysis of the mechanical processes related to fluid injection-induced seismicity. Although it is widely observed that slip induces surface deformation, it often receives less attention as a source of surface deformation in geothermal field because the energy released by a single seismic event is insufficient to induce the observed surface deformation (typically several centimeters of subsidence per year). For example, the Okada model indicates that the maximum deformation induced by the largest micro-seismicity at the Newberry project (fault surface area 62,500 m^2 with 2.3 mm slip at depth 2500 m (Fang et al., 2015B)) would be a vertical displacement of 0.006 mm and surface tilt of 3.5 nano-radians, respectively, of which only the tilt signal is marginally resolvable with current instruments (**Fig. 7**).

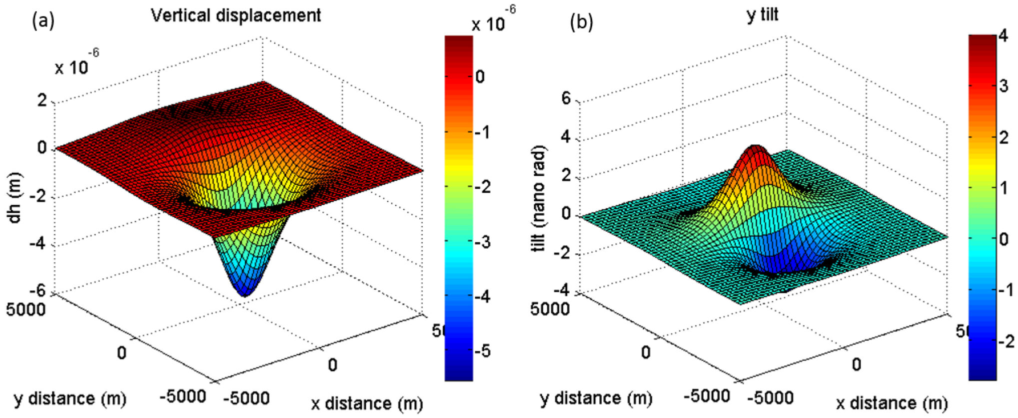

Figure 7. Surface deformation for the largest micro-seismic event detected at the Newberry EGS stimulation. (a) Vertical displacement and (b) tilt along the y-direction. Rectangular source 250 m × 250 m at a dip of 60° dipping in the y-direction centered at a depth of 2500 m and with 2.3 mm of shear offset (Fang et. al., 2015).

When describing fault reactivation by fluid injection, however, it is inappropriate to consider solely each individual seismic event; rather, cumulative displacement may be recovered from repeating events on the same fault or from slip that occurs aseismically. For instance, the shear offset observed across one borehole at the Soultz geothermal experiment was significantly larger than the expected slip calculated from the contributing seismic events (Cornet et al., 1997). More directly, observations of injection induced shear slip offset are typically far larger than the slip calculated from induced seismicity (Guglielmi et. at. 2015a&b). This result might be explained by two mechanisms: (i) stacking of seismic fault events within a fault zone and (ii) aseismic or slow-slip fault reactivation. The first mechanism has often been observed and simulated in the development of injection-induced seismicity (Horton 2012, McClure 2013, Gischig 2015), while the second mechanism is reviewed and discussed for tectonic plate boundary slip (Peng and Gomberg 2010) and with injection triggered fault slip (Zoback and Gorelick 2012, Guglielmi et al., 2015a&b).

Another interesting observation of direct slip measurements by Guglielmi et al. (2015a&b) is that the slip front (fracture tip) is always ahead of the fluid-pressurized front. Similar behavior is observed in numerical simulations of induced slip (Gischig, 2015). The slip front should be evaluated from the force balance of the slip driving stress (induced by effective normal stress reduction) within the pressure (and/or thermal) front and the resisting stress (friction) between pressure front and slip front. Thus the slip front in fault reactivation is always ahead of the pressure (and/or thermal) front and the size and magnitude of slip is strongly dependent on the orientation and frictional properties of the fault. This behavior shows that a larger slip zone can be generated by a smaller area of stress perturbation increasing the likelihood of a large event.

Fig. 8 shows the relationships between fault size and maximum magnitude of surface deformations calculated by an Okada solution assuming a rectangular fault at a depth 2500 m with a 60º dip. It indicates that the magnitude of surface deformation increases with both fault size and shear offset. In fact, the fault size and slip distance are mutually dependent. Assuming constant stress drop across the fault, the larger the area of the fault, the larger the shear offset (Zoback and Gorelick 2012). Accordingly, it is expected that a sizable area of fault slip would generate detectable surface deformation signals. The Okada slip solution (**Fig. 8)** indicates that for a 200 m×200 m fault at depth 2500 m, even several millimeters of slip can be detected with tilt- and strain-meters.

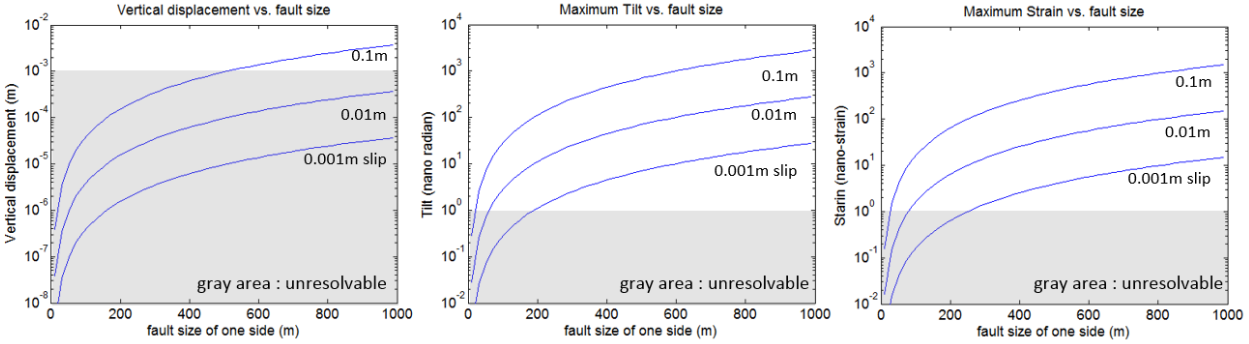

Figure 8. Maximum magnitude of surface deformation *vs.* fault size (length of one side of rectangular fault) with three slip distances (0.001 m, 0.01 m and 0.1 m) at a depth 2500 m. The magnitude of surface deformation increases with both fault area and total slip.

The Okada model assumes a finite rectangular slip source with uniform displacement embedded within an elastic half-space (Okada, 1985). The behavior of the resulting surface deformation depends on the geometry of the source including width, height and angle of dip. For example, the symmetry of the surface deformation is controlled by the fault dip. The maximum symmetry with respect to the horizontal fault direction is achieved at 45° dip, while maximum asymmetry is achieved at 0° or 90°. **Fig. 9** illustrates the fault geometry used in our analysis. The rectangular fault has a horizontal length of 1000 m and width along the slip direction of 500 m dipping at 60° and embedded in an elastic medium with a Poisson's ratio of 0.25 Although the fault geometry is chosen arbitrarily, a fault of this size, geometry, and orientation would be reasonable to expect within a geothermal reservoir.

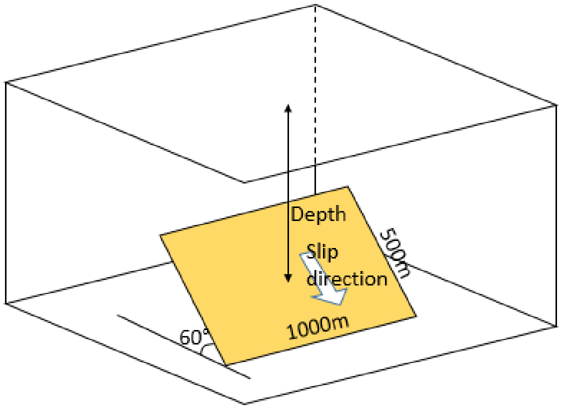

Figure 9. Fault geometry used here with the yellow rectangle representing a slip surface with a dip angle of 60°, horizontal length of 1000 m and width (along slip direction) of 500 m. Depth to the surface is variable.

2.3 Summary of Surface Deformation

Maximum surface deformation calculated by the Mogi and Okada models, with fixed source geometry and with various volume changes and shear offsets, are shown in **Fig. 10**. The gray area represents signals that are undetectable with current geodetic techniques (~1 mm vertical displacement, ~1 nano-radian and ~1 nano-strain). The equivalent heat production period is specified in parentheses in the plots (a1), (a2) and (a3) assuming coupled spherical deformation with Q_f=0.1m^3/s, α=5×10^{-5}/K, $(\rho_f C_f)/(\rho_r C_r)$=2, E_{host}=E_{res}, ν=0.25 and ΔT=100°C. Also the equivalent moment magnitude with a shear modulus 15 GPa is noted in parentheses in the plots (b1), (b2) and (b3). In all cases, a detailed deconvolution of subsurface deformation can be achieved by tilt and strain but not generally through measurement of vertical displacements. For example, a volume change of 10^3 m^3 (20 days of geothermal operation) is not resolvable by vertical displacement for any source depth deeper than 1000 m, while it remains resolvable in both tilt and strain. Similarly, 1 mm to 1 cm of slip is undetectable in vertical displacement, but it is readily detectable with tilt and strain.

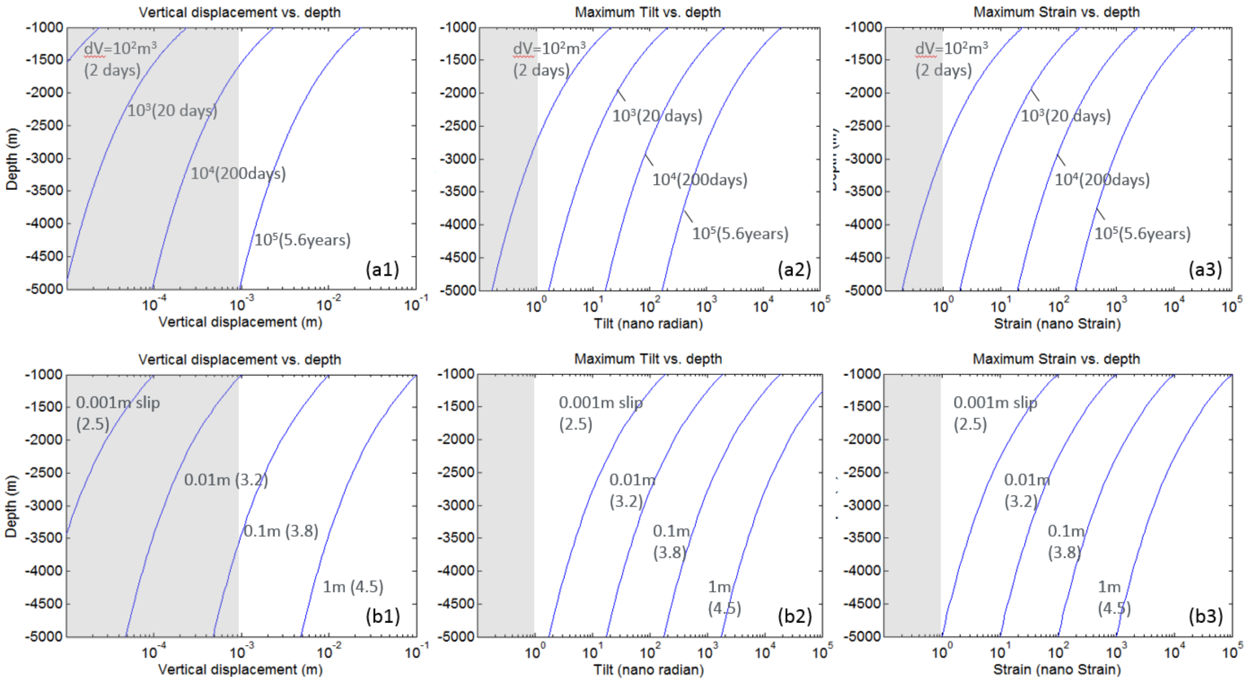

Figure 10. Log-linear plot of maximum surface deformations induced by various contractile volume changes and by shear slip. (a1): maximum vertical displacement from contractile volume change. (b1) maximum vertical displacement from shear slip. (a2): maximum tilt from contractile volume change. (b2) maximum tilt from shear slip. (a3): maximum radial strain from contractile volume change. (b3) maximum horizontal strain from shear slip. Geometry assumed for the slip solution is shown in Fig. 4. The parenthesis in volume change (a1, a2 and a3) denotes equivalent period for heat production of Q_f=0.1 m^3/s, $\alpha=5\times10^{-5}$ /K, $(\rho_f C_f)/(\rho_r C_r)=2$, $E_{host}=E_{res}$, Poisson's ratio 0.25 and ΔT=100°C (same assumption with Fig. 3 except constant temperature difference). The parentheses for shear slip (b1, b2 and b3) denote the equivalent single event magnitude. In all cases, tilt and strain show significantly lower detection limits than achievable using surface standard displacement measurements.

Since both volume change and slip induces surface deformation concurrently, it is necessary to distinguish the causal mechanism from observed surface deformation. One indication of different contributing mechanisms would be the timing of the events. In general, it is presumed that shear slip events would be episodic and staccato, while the volume change signal due to energy extraction would be more continuous and gradual. In addition, dilatation and slip may be further distinguished by their surface deformation patterns – slip induces a more spatially compact and asymmetric form of surface deformation.

Fig 11 represents a comparison of the shape profiles induced by slip (red) and volume change (blue). Three different vertical displacement profiles (from the volume changes at two depths of 1400 m and 2500 m and from slip at a depth 2500 m) are plotted in **Fig 11 (a)**. For comparison, the magnitude of all three deformations are fixed to have the same maximum vertical displacement at the surface. The figure clearly shows that the shear events (red solid line) yield more intense and asymmetric surface deformation than the deformation induced by volume change at the same depth (blue solid line). The ratio of maximum vertical displacement and tilt of the Mogi volume solution and Okada slip solution are plotted in **Fig. 11 (c),** which further emphasizes the difference in surface deformation arising from these distinct mechanisms.

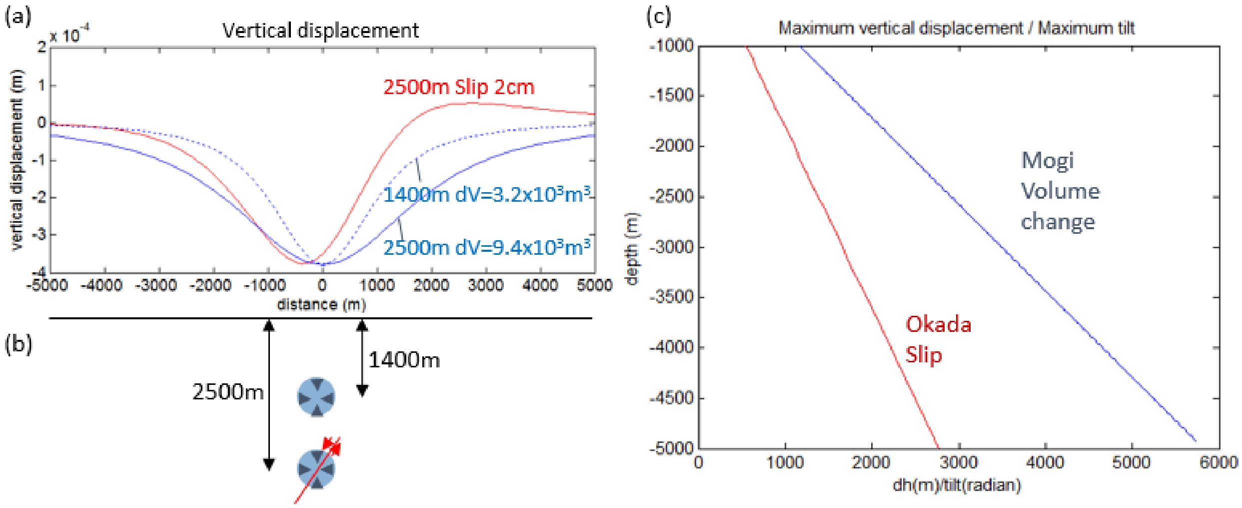

Figure 11. (a): Vertical displacement profile induced by (b) Mogi and Okada slip sources. Red profile in (a) is Okada slip solution of 2 cm slip at depth 2500 m with a fault geometry as **Fig. 9**. Blue lines denote Mogi volume change solution at depth 2500 m (solid line) and 1400 m (dashed line). For comparison, all source magnitudes are fixed to yield the same maximum surface displacement. Okada slip source (red solid line) yields a more narrow and asymmetric surface deformation pattern than the Mogi source (blue solid line). In addition, the deformation profile of Okada slip at depth 2500 m is similar to the deformation profile of the Mogi volume change at depth 1400 m (blue dashed line). Figure (c) plots of maximum vertical displacement divided by maximum tilt *vs.* depth. This demonstrates that the ratio of maximum vertical displacement and maximum tilt for an Okada slip dislocation is ~2x that of the Mogi source.

3. Field Data and Discussion

Surface deformations have been observed at a variety of geothermal reservoirs using near-surface tilt and surface displacements measured by InSAR. Tilt measurement data are available for two reservoirs in Japan, namely, the Hijiori injection test site and the Okuaizu geothermal field (Vasco et al., 2002). In addition, InSAR vertical displacements are available from various geothermal fields: Brady Hot Springs, Coso, Dixie Valley, Salton Sea, San Emidio (Ali et al., 2014; Eneva et al., 2012; Falorni et al., 2011; Fialko and Simons, 2000; Foxall and Vasco, 2003; Vasco et al., 2002; Vasco 2013). The critical advantages of tilt observations over InSAR-inferred displacement measurements are the low detection limit (high sensitivity) and dense temporal sampling, which allows the recovery of a detailed record of short-term behavior. InSAR methods, in contrast, have a higher detection limit (lower sensitivity) for imaging subsurface deformation as deduced from vertical displacement (**Fig. 10**). However, the relatively low cost of InSAR data and processing and its ability to produce synoptic surface deformation images makes this technique attractive and therefore widely used.

The magnitude of thermal contraction in geothermal fields can be estimated by energy extraction rate. Assuming a conversion efficiency of 10% from thermal recovery to electrical conversion (including running at sub-capacity), the total heat energy extracted at 1 MW for 1 year from a geothermal field is $\sim 3.15\times10^{14}$ J. Using this conversion scenario and rock properties assumed as $\alpha_v=5\times10^{-5}$, density 2700 kg/m^3 and specific heat of 900 J/kg·K with a deformation ratio of 0.56 ($E_{host}=E_{res}$, $\nu=0.25$), allows the inference that 1 MW geothermal operation for 1 year induces $\sim 3.63\times10^{3}$ m^3 of subsurface volume change. We compare the magnitudes of expected maximum surface deformation due to thermal contraction to the observed maximum vertical displacement (Brady Hot Springs, Coso and Dixie Valley) and tilt (Hijiori and Okuaizu) in **Fig. 12**. In order to calculate the subsurface volume change, we used current (2014) capacities for the operating fields (Brady Hot Springs, Coso, Dixie Valley and Okuaizu) and total injected volume for the period of observation in the Hijiori injection test. Our results show that observations at Brady Hot Springs and Coso show similar or slightly smaller than predicted surface deformations. In contrast, surface deformations observed at Dixie Valley, Okuaizu and Hijiori are considerably larger than expected. The observed smaller surface deformations are straightforward to explain because: (i) we use current (2014) maximum operational capacity, which may be larger than the actual capacity over the same period; (ii) only a single Mogi source is modeled for each example; and (iii) decoupling of the spherical reservoir from the elastic crust is not considered. Accordingly, result of smaller surface deformation observations than predicted in the Brady Hot Springs and Coso geothermal fields are both easily explicable and, moreover, the similarities of their magnitudes implies that thermal contraction plays a significant role in inducing the large observed surface deformations. The results for Dixie Valley, Okuaizu and Hijiori, however, clearly show the need for another significant deformation source in addition to thermal contraction of a spherical reservoir. Considering the extensive network of faults (typically several kilometers in horizontal extension) in these reservoirs, the large deformations suggest the necessary involvement of systematic shear reactivation in inducing the large surface deformations.

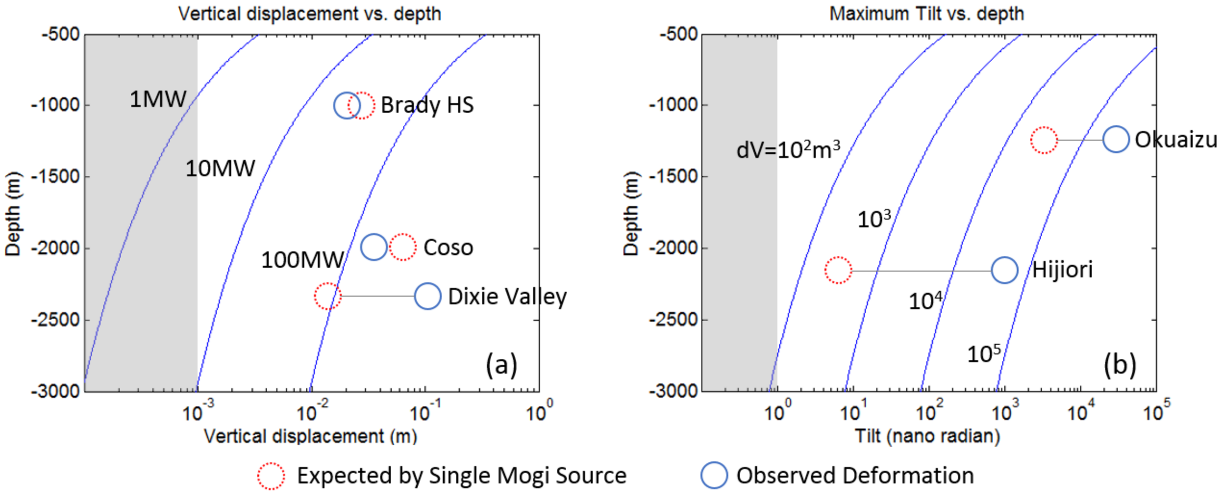

Figure. 12. Comparison of expected maximum surface deformation due to thermal contraction (red dashed circles) and observed maximum deformation (blue solid circle). The large gap between predicted and observed values in Dixie Valley, Okuaizu and Hijiori implies the probable involvement of shear offset to produce the large observed surface deformation.

We further note that the inversion of surface deformation to constrain subsurface volume changes often requires a shallow depth for the deformation source; for example, this is the case for Hijiori, Okuizu, Brady Hot Springs and Dixie Valley (Vasco et al., 2002; Ali et al., 2016; Foxall and Vasco, 2003). In fact, slip on finite planar faults may also explain the observation of a shallow source – dislocation slip on planar faults produces more intense surface deformation than shallower volume changes from a spherical source (**Fig. 11**), and fluid-pressure-induced fault reactivation is favored at shallow depths (Fang et al., 2015) because of lithostatic stress profiles within the upper crust.

4. Summary and Conclusions

We have reviewed and modeled surface deformation induced by cold-water injection in geothermal reservoirs through constrained isotropic volume change and injection-induced shear offset. The Mogi and Okada solutions developed here indicate that surface deformation associated with these processes, particularly those manifest as tilt and strain, can be readily detected with existing geodetic instruments and thus monitored in some detail. We assess spherical thermal contraction within the surrounding rock and illustrate the mechanism of permeability increase by cooling. Although constrained deformation and reservoir decoupling reduce the signal and thus limit maximum observable deformation, these are still sufficiently large to be resolved and deconvolved to describe reservoir behavior. For fully coupled deformation, thermal contraction induced by 20 days of heat production at a flow rate of 0.1 m^3/s and temperature difference of 100°C is resolvable for any source depth shallower than 5000 m (other assumptions: $\alpha=5\times10^{-5}$ /K, $(\rho_f C_f)/(\rho_r C_r)=2$, $E_{host}=E_{res}$ and $v=0.25$). If the source depth is 2500 m, then this would induce over 10 nano-radians and 10 nano-strains of deformation, both of which are more than 10 times larger the minimum detection limit of current geodetic instruments (tiltmeters and strainmeters). If the far field stress is 50 MPa and the bulk modulus of the reservoir rock is 20 GPa, the assumption of coupled deformation is fully valid up to a thermal drawdown of 100°C (the system decouples at ΔT of ~110ºC). Furthermore, simple one-dimensional flow models illustrate that subsurface thermal drawdown behavior can be monitored and described in detail with surface or near-surface geodesy.

In addition to volumetric deformation, an Okada slip dislocation model shows that surface deformations induced by fault reactivation have sufficient magnitude to be detected and monitored by surface geodesy in geothermal fields. Energy release from a single seismic event (as commonly observed in geothermal fields) is generally insufficient to induce large surface deformations, although repeated seismic and aseismic fault reactivations could generate a considerable net shear offset for a sizable fault surface, allowing it to be detected from surface geodesy. For example, 1 mm slip offset on a 1000 m×500 m fault dipping at 60° at a center depth of 2500 m will induce a signal of ~10 nano-radians and ~10 nano-strains , which are well above instrumental detection limits.

Significant surface deformations have been observed at active geothermal sites both with tiltmeters and with InSAR. Considering heat production rates and sizes of putative subsurface faults, the observed large surface deformation is likely the result of the combined influence of both thermal contraction and slip offset. Although the two mechanisms may act concurrently to produce surface deformation, their respective influence may be deconvolved from the temporal and spatial variation of the surface deformation. Geodetic measurements have a high potential to successfully image geothermal reservoirs, which in turn may be useful in understanding the evolution of their permeability structure.

Acknowledgements

This work is a partial result of support provided by DOE Grant DE-EE0006761. This support is gratefully acknowledged.

References

Ali, S.T., Akerley, J., Baluyut, E.C., Cardiff, M., Davatzes, N.C., Feigl, K.L., Foxall, W., Fratta, D., Mellors, R.J., Spielman, P., Wang, H.F., and Zemach, E., 2016, Time-series analysis of surface deformation at Brady Hot Springs geothermal field (Nevada) using interferometric synthetic aperture radar: Geothermics, v. 61, p. 114–120, doi: 10.1016/j.geothermics.2016.01.008.

Cooper, H.W., and Simmons, G., 1977, The effect of cracks on the thermal expansion of rocks: Earth and Planetary Science Letters, v. 36, p. 404–412.

Cornet, F.H., Helm, J., Poitrenaud, H., and Etchecopar, a., 1997, Seismic and Aseismic Slips Induced by Large-scale Fluid Injections: Pure and Applied Geophysics, v. 150, p. 563–583, doi: 10.1007/s000240050093.

Dempsey, D., and Suckale, J., 2015, Induced Earthquake Sequences in Geothermal Settings : Data Trends and Modeling Approaches: Proceedings: Fortieth Workshop on Geothermal Reservoir Engineering Stanford University, Stanford, California. January 26-28,.

Ellsworth, W., 2013, Injection-Induced Earthquakes: Science, v. 341, p. 250–260, doi: 10.1785/gssrl.83.2.250.

Elsworth, D., 2001, Mechanical response of lined and unlined heated drifts: Rock Mechanics and Rock Engineering, v. 34, p. 201–215, doi: 10.1007/s006030170009.

Elsworth, D., Mattioli, G., Taron, J., Voight, B., and Herd, R., 2008, Implications of magma transfer between multiple reservoirs on eruption cycling: Science, v. 322, p. 246–248.

Eneva, M., and Adams, D., 2012, Surface deformation in Imperial Valley, CA, from satellite radar interferometry: Geoth. Resour, v. 36, p. 1339–1344.

Eneva, M., Falorni, G., Teplow, W., Morgan, J., Rhodes, G., and Adams, D., 2011, Surface deformation at the San Emidio geothermal field, Nevada, from satellite radar interferometry: Geothermal Resources Council Transactions, v. 35, p. 1647–1653.

Eshelby, J., 1957, The determination of the elastic field of an ellipsoidal inclusion, and related problems: Proceedings of the Royal Society,.

Falorni, G., Morgan, J., and Eneva, M., 2011, Advanced InSAR Techniques for Geothermal Exploration and Production: GRC Transactions, v. 35.

Fang, Y., Elsworth, D., and Cladouhos, T., 2015A, Estimating In-Situ Permeability of Stimulated EGS Reservoirs Using MEQ Moment Magnitude : an Analysis of Newberry MEQ Data: Proceedings : Fortieth Workshop on Geothermal Reservoir Engineering Stanford University, Stanford, California. January 26-28,.

Fang, Y., Hartog, S., Elsworth, D., Marone, C. and Cladouhos., T., 2015B, Anomalous distribution of microearthquakes in the Newberry Geothermal Reservoir: Mechanisms and implications. Geothermics.

Fialko, Y., and Simons, M., 2000, Deformation and seismicity in the Coso geothermal area, Inyo County, California: Observations and modeling using satellite radar interferometry: Journal of Geophysical Research, v. 105, p. 21781, doi: 10.1029/2000JB900169.

Foxall, B., and Vasco, D., 2003, Inversion of Synthetic Aperture Radar Interferograms for Sources of Production-Related Subsidence at the Dixie Valley Geothermal Field: Proceedings :

Twenty-eighth Workshop on Geothermal Reservoir Engineering Stanford University, Stanford, California. January 27-29.

Gan, Q., and Elsworth, D., 2014, Analysis of fluid injection-induced fault reactivation and seismic slip in geothermal reservoirs.: Journal of Geophysical Research : Solid Earth, p. 3340–3353, doi: 10.1002/2013JB010679.

Geothermal Energy Association, 2014, 2014 Annual U.S. & Global Geothermal Power Production Report

Gischig, V.S., 2015, Rupture propagation behavior and the largest possible earthquake induced by fluid injection into deep reservoirs: Geophysical Research Letters, p. 7420–7428, doi: 10.1002/2015GL065072.

Goodman, R., 1980, Introduction to rock mechanics, John Wiley & Sons.

Guglielmi, Y., Cappa, F., Avouac, J., Henry, P., and Elsworth, D., 2015a, Seismicity triggered by fluid injection – induced aseismic slip: Science, v. 348, p. 1224–1226.

Guglielmi, Y., Elsworth, D., Cappa, F., Henry, P., Gout, C., Dick, P., and Durand, J., 2015a, Insitu observations on the coupling between hydraulic diffusivity and displacements during fault reactivation in shales: Journal of Geophysical Research : Solid Earth, p. 1–23, doi: 10.1002/2014JB011237.

Horton, S., 2012, Disposal of Hydrofracking Waste Fluid by Injection into Subsurface Aquifers Triggers Earthquake Swarm in Central Arkansas with Potential for Damaging Earthquake: Seismological Research Letters, v. 83, p. 250–260, doi: 10.1785/gssrl.83.2.250.

Im, K., Elsworth, D., Guglielmi, Y., and Mattioli, G., 2015, Use of Geodesy to Discriminate the Deformation Mechanics in EGS Reservoir, Proceedings 49th US Rock Mechanics/Geomechanics Symposium.

Jung, R., 2013, Provisional chapter EGS — Goodbye or Back to the Future: InTech. http://dx.doi.org/10.5772/56458, p. 95–121, doi: 10.5772/56458.

Majer, E.L., Baria, R., Stark, M., Oates, S., Bommer, J., Smith, B., and Asanuma, H., 2007, Induced seismicity associated with Enhanced Geothermal Systems: Geothermics, v. 36, p. 185–222, doi: 10.1016/j.geothermics.2007.03.003.

McClure, M.W., and Horne, R.N., 2013, Discrete Fracture Network Modeling of Hydraulic Stimulation, Springer.

Mogi, K., 1958, Relations between the eruptions of various volcanoes and the deformations of the ground surface around them, Bull. Earthquake Res. Inst. Univ. Tokyo, 36, 99– 134

Norbeck, J., and Horne, R., 2015, Injection-Triggered Seismicity: An Investigation of Porothermoelastic Effects Using a Rate-and- State Earthquake Model: Proceedings : Fortieth Workshop on Geothermal Reservoir Engineering Stanford University, Stanford, California. January 26-28,.

Okada, 1985, Surface deformation due to shear and tensile faults in a half-space: International Journal of Rock Mechanics and Mining Sciences Geomechanics Abstracts, v. 75, p. 1135–1154, doi: 10.1016/0148-9062(86)90674-1.

Peng, Z., and Gomberg, J., 2010, An integrated perspective of the continuum between earthquakes and slow-slip phenomena: Nature Geoscience, v. 3, p. 599–607, doi: 10.1038/ngeo940.

Scholz, C.H., 1998, Earthquakes and friction laws: Nature, v. 391, p. 37–42, doi: 10.1038/34097.

Segall, P., and Fitzgerald, S.D., 1998, A note on induced stress changes in hydrocarbon and geothermal reservoirs: Tectonophysics, v. 289, p. 117–128, doi: 10.1016/S0040-1951(97)00311-9.

Vasco, D.W., Karasaki, K., and Nakagome, O., 2002, Monitoring production using surface deformation: The Hijiori test site and the Okuaizu geothermal field, Japan: Geothermics, v. 31, p. 303–342, doi: 10.1016/S0375-6505(01)00036-0.

Vasco, D.W., Rutqvist, J., Ferretti, A., Rucci, A., Bellotti, F., Dobson, P., Oldenburg, C., Garcia, J., Walters, M., and Hartline, C., 2013, Monitoring deformation at the Geysers geothermal field, California using C-band and X-band interferometric synthetic aperture radar: Geophysical Research Letters, v. 40, p. 2567–2572, doi: 10.1002/grl.50314.

Vasco, D., Wicks, C., Karasaki, K. and Marques O., 2002, Geodetic Imaging: Reservoir monitoring using satellite interferometry: Geophysical Journal International, v149., p. 555–571. doi: 10.1046/j.1365-246X.2002.01569.x

Zarrouk, S.J., and Moon, H., 2014, Efficiency of geothermal power plants: A worldwide review: Geothermics, v. 51, p. 142–153, doi: 10.1016/j.geothermics.2013.11.001.

Zoback, M.D., Kohli, A., Das, I., and McClure, M., 2012, The Importance of Slow Slip on Faults During Hydraulic Fracturing Stimulation of Shale Gas Reservoirs: Spe 155476, p. SPE 155476, doi: 10.2118/155476-MS.

Zoback, M.D., and Gorelick, S.M., 2012, Earthquake triggering and large-scale geologic storage of carbon dioxide: Proceedings of the National Academy of Sciences, v. 109, p. 10164–10168, doi: 10.1073/pnas.1202473109.

PART II: THE HOT HPP TOOL: CHARACTERIZING THE EVOLUTION OF STRESS AND PERMEABILITY AND DESIGN FOR HTHP CONDITIONS

Derek Elsworth, Kyungjae Im
Energy and Mineral Engineering, EMS Energy Institute and G3 Center, Pennsylvania State University
Yves Guglielmi
[1]Lawrence Berkeley National Laboratory

TABLE OF CONTENTS

Abstract

In Situ Measurements with the Hot HPP Tool: The success of EGS requires both high-fluid-throughput and thermally-long-lived geothermal reservoirs. High-fluid-throughput in traditional basement rocks requires that reservoir permeabilities at depth (~5km) must be elevated from the microDarcy to the milliDarcy range and with long thermal life. A long-thermal life requires that high heat-transfer area is maintained concurrent with high flow rates. This is only feasible if fluid circulation in the reservoir has a broad and even sweep through media with a short thermal diffusion length (small fracture spacing) thus avoiding thermal short-circuiting and damaging feedbacks of thermal permeability enhancement. Therefore permeability control is a key requirement to develop a successful EGS reservoir. Thermally-driven permeability evolution results from induced strains around fractures that, in turn, result from temperature change. These deformations are strongly dependent on parameters of the fluid and rock such as thermal expansion coefficient, thermal conductivities, flow rate, fracture stiffness and *in situ* stress field. Measuring and analyzing the deformations together with permeability evolution *in situ* will describe fluid flow and conductive thermal energy transport in the reservoir and provide essential parameters to effectively develop EGS reservoirs. Such direct measurements of fracture deformation with permeability evolution have been successfully conducted with the unique hydraulic pulse protocol (HPP) probe (Guglielmi et. al. 2015 a&b). However, the current tool is limited to ~10 MPa and

80°C and not yet readily applicable to a high pressure high temperature environment. Here we explore the potential developments needed to elevate tool performance to 100 MPa and 300°C and necessary experimental protocols to maximize data recovered. In this work we examine (i) expected fracture deformation and recoverable HPP tool signals in an EGS system and (ii) a strategy to upgrade the current HPP tool to be stable in an HTHP environment. Deformations from cold water flow into a fracture and the expected HPP response of the tool are investigated by numerical simulations. These results indicate that there are two modalities of deformation: (i) immediate (<10 seconds) pressure-driven dilation of the fault/fracture and (ii) a second delayed thermally-induced response of opening and slip. Observed deformations are analyzed with the theory for a soft inclusion (Eshelby, 1957) and indicate that thermally-induced unloading and consequent deformations are strongly dependent on the hydro-thermal-mechanical properties of the reservoir and fracture. Stress evolution and its magnitude is determined by the morphology of the cooled volume. A flat cooling ellipsoid centered on the fracture results in thermal cracking (opening in the direction normal to the fracture) while fracture opening enlarges as cooling proceeds. We show that the stress field in the chilled inclusion can be approximated by the temperature change without considering the external thermal gradient. The analysis of cold water injection for one month (fracture zone of 4mm thickness and 10 Darcy permeability) resulted in ~3 mm of opening and ~6mm of slip. Expected HPP signals (deformations at ~30cm above the isolated fracture) are significantly larger than tool resolution confirming the utility of the tool to precisely measure the hydro-thermal-mechanical properties of the reservoir and to describe reservoir deformation behavior. Shear displacement signals are nearly identical to fracture surface deformation while normal displacement initially diverges from fracture opening reflecting thermal contraction of the reservoir between anchor and fracture surface.

Tool Design: We review current cold-HPP tool capabilities and required upgrades for deployment in geothermal systems. The current displacement measurement system (fiber Bragg grating) is fundamentally stable at HTHP conditions while the deformation cage and current packer system are not. The deformation cage itself may not require significant modification in design except the aluminum body and cage-fiber adhesive may need to be replaced by materials with a high durability to elevated temperature. Current neoprene packers will not survive and considerable modification in design is needed. Existing HTHP off-the-shelf packers are reviewed and requisite revisions to adopt the packer mechanism in the current HPP tool are discussed.

1. Introduction

The success of EGS requires that high-fluid-throughput and thermally-long-lived geothermal reservoirs may be universally engineered and developed, at will. High-fluid-throughput in traditional basement rocks necessitates that reservoir permeabilities at depth (~5 km) must be elevated from the microDarcy to the milliDarcy range – this avoids untenable pumping costs and avoids inadvertently fracturing the reservoir by extreme fluid overpressures. Although fracturing would appear desirable in developing conduits with high-fluid-throughput, it typically violates the second tenet of a desired long thermal life. A long-thermal life requires that high heat-transfer area is maintained concurrent with high flow rates. This is only feasible if fluid circulation in the reservoir has a broad and even sweep through media with a short thermal diffusion length (small fracture spacing) thus avoiding short-circuiting and damaging feedbacks of thermal permeability enhancement.

Key needs in the successful development of EGS reservoirs are to (i) stimulate sufficient permeability to enable high mass flow rates while (ii) simultaneously retaining high heat transfer area *via* broad fluid sweep through the reservoir. This is straightforward in conventional geothermal reservoirs where initial permeabilities are both high (yielding high flow rates), broadly distributed, largely uniform and with relatively low sensitivity to changes in fluid pressure and hence effective stresses. This allows broad thermal sweep through the reservoir and muted feedback towards flow localization. However, the converse is true in EGS reservoirs – they begin with low permeabilities, must be stimulated to develop sufficient flow rates, and are then extraordinarily sensitive to flow-localization through the combined influence of fluid pressures and especially the reinforcing feedback of thermal-drawdown-induced stresses.

In situ tests that can both make initial measurements of reservoir properties (permeability, frictional strength and stability….) and state (stress, pressure, chemical potential….) and constrain functional impacts of changes in temperature, pressure and deformation (THM) at prototype scale are crucial in projecting the evolution of the reservoir. Each of these characterizations requires an innate understanding of the strength and nature (reinforcing or ameliorating) of the feedbacks between permeability (H) and deformation (M) or seismicity, and the complicating role of ancillary factors such as temperature (T).

Hydro-mechanical (HM) deformation response has been successfully characterized with permeability in field scale fault pressurization studies (Guglielmi et. at. 2015 a&b) with the unique borehole tool – the Hydraulic Pulse Protocol (HPP) tool. In such experiments, fracture dilation responds to applied pressures and measured injection rate and concurrent histories of displacement in normal and slip modes are clearly recorded. The current "cold-HPP" tool, however, has only been qualified in 20-to-50 m deep open boreholes, injection pressures up to 6 MPa and temperatures to 20°C. Therefore, an upgrade is mandated to deploy the tool in representative EGS systems.

Thus, in this study, we assess the recoverable signals feasible from a hot-HPP tool and review the required upgrades to design for a hot EGS system. We first investigate anticipated fracture deformation signals resulting from cold water injection into a hydraulically isolated single fracture in a hot reservoir. We analyze the evolution of thermal stress/strain using the concept of an Eshelby inclusion and then recover the expected fracture deformation and HPP tool signal from numerical simulation. We then discuss the design of a high-temperature/high-pressure version of the HPP borehole tool – the Hot-HPP – to extend the range of the Cold-HPP-Tool from 6 MPa/70°C to 100 MPa/>150°C-to-<300°C – suitable for deployment in typical EGS geothermal wells

2. Protocols for In Situ Measurement

The HPP tool enables the measurement of (i) *in situ* stresses, and the dependencies of permeability on (ii) stress and (iii) temperature (THM). In all cases, the tool straddles a fracture that the borehole pierces with a hydraulically-isolated (packed-off) zone that may be pressurized. The testing perturbation is applied as a fluid pressure pulse in the isolated zone that may propagate into the formation and fault zone. The prescribed pressure history and related changes in the effective stresses and measured flowrates under prescribed injection pressures may be used to define the evolution of permeability with applied effective stress and monitored fracture dilation and displacement. Fluid-pressure-prescribed differential temperature (relative to the reservoir temperature) may be used to follow the evolution of permeability under thermal conditions and to follow themomechanical influences. Here we analyze the expected response of the HPP tool from pressure and temperature perturbations by both analytic and numerical methods.

2.1 Thermal Stress Evolution with Cold Water Injection

As discussed in Part I, thermally-induced stresses in geothermal reservoirs are typically large enough to surpass fluid pressure driven effects and may consequently induce tensional decoupling. Moreover, thermal stress evolves quasi-continuously and uniformly until the reservoir is thermally depleted while pressures are typically localized near the wellbore and bounded by injection and production pressures. Therefore although permeability evolution is initially generated by fluid pressurization, the following thermal unloading applies significant and continuous influence on permeability through the termination of geothermal field operations.

In an infinite elastic medium, the stress/strain change within an inclusion can be represented by the Eshelby solution. Eshelby (1957) presented a the change in strain in a homogeneous infinite medium ε^c as,

$$\varepsilon^c{}_{ij} = S_{ijkl}\varepsilon^*{}_{kl} \tag{31}$$

where, S_{ijkl} is the Eshelby tensor and ε^* represents an unconfined environment. In an unconfined uniform system, all thermal shear strains are zero ($\varepsilon^*{}_{ij}=\varepsilon^*{}_{jk}=\varepsilon^*{}_{ki}=0$) and normal strains are identical to the linear thermal strain. Therefore

$$\varepsilon^*{}_{ii} = \frac{1}{3}\alpha_v \Delta T \tag{32}$$

where, α_v is the volumetric thermal expansion coefficient and ΔT is temperature change.

Stress change induced by confined deformation (**Eqn (1)**) can be represented as,

$$\Delta\sigma_{ij} = C_{ijkl}(\varepsilon^c{}_{kl} - \varepsilon^*{}_{kl}) \tag{33}$$

where C_{ijkl} is the elasticity tensor.

The Eshelby tensor S_{ijkl} is dependent on the shape of the inclusion. **Fig. 1** represents ratios between the Eshelby inclusion solution and unconfined deformation of strain and stress changes of different aspect ratios (*b/a*) of a spheroid in an infinite medium with a Poisson ratio ν=0.2. Here '*a*' denotes the long axis of the spheroid (horizontal) and '*b*' denotes the short axis (vertical) (see **plot A**). The resulting plots illustrate that when the inclusion is spherical ($b/a=1$), both stress and strain are approximately half of the unconfined value in all directions (the value depends on the Poisson ratio). Conversely, if the spheroid is flatter ($b/a<1$) then horizontal strain decreases and eventually becomes null, while vertical strain increases. Stress change responds in the opposite sense to strain such that a smaller strain change induces a higher stress change (See **Eqn (3)**).

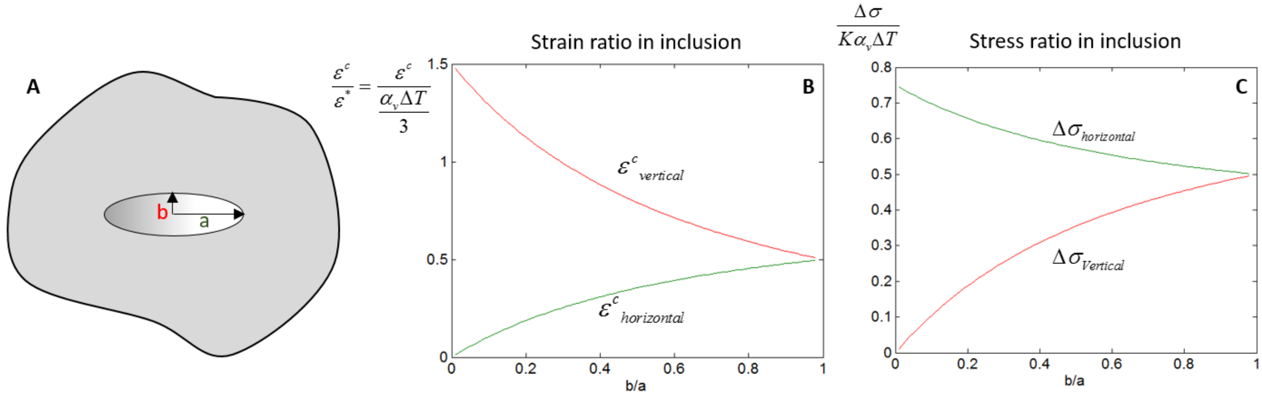

Figure 1. **A**: Inclusion geometry. **B**: Ratio between confined (Eshelby) Strain and unconfined strain. **C**: Ratio between confined (Eshelby) stress change and unconfined stress change.

Fig. 2 shows the magnitude of thermal unloading recovered from the Eshelby solution. The green curve denotes the horizontal unloading and the red line denotes the vertical unloading induced by a temperature change. Results are in terms of the ratios of vertical and horizontal length of the cooled spheroid (same as **Fig 1**). Smaller (<< 1) ratios represent a flat geometry and unity represents a sphere. The plot shows that if cooling around a fracture is flat ($b<<a$), then the stress reduction mostly occurs in the horizontal direction. Conversely, if the cooling is spherical ($b\sim a$) then both the horizontal and vertical unloading become similar in magnitude.

The calculated magnitude of the thermal stress change is significant, implying the likelihood of the evolution of a tensional stress and therefore the generation of a substantial change in permeability. For example, a stress change due to spherical cooling at ΔT=200°C induces a stress reduction of ~90 MPa. This is typically larger than the maximum *in situ* stress in geothermal reservoirs. The result shows that there is a considerable likelihood of the development of tensional stresses and in resulting fracture dilation and permeability increase. Induced tensional stresses generate two significant behaviors as illustrated in **Fig 2 (**left side**)** that: (i) horizontal unloading around the fracture may induce thermal cracking and (ii) vertical unloading may induce tensional opening. Note that the induced stress field is strongly dependent on the shape of cooling. Thermal cracking (cracks normal to the fracture) will be dominant when the shape of the cooling ellipsoid is flat and the fracture opening will become significant later as the cooling evolves to spherical shape. This observation of the "cooled-shape" dependency of the stress, strain and permeability response implies that both thermal conductivity and fluid flow rate are important properties in defining permeability evolution.

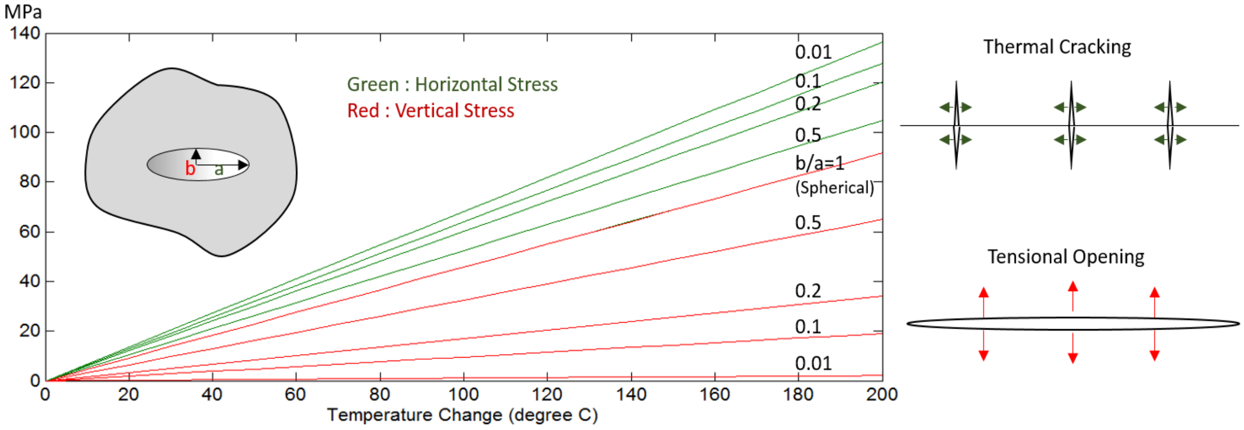

Figure 2. Thermal unloading evaluated from the Eshelby solution. Input parameters are: bulk modulus K=30GPa, Poisson ratio v=0.2 and volumetric thermal expansion coefficient $\alpha_v=3\times10^{-5}$. The two illustrations (right) show schematic deformation patterns when stresses around a fracture become extensional.

As briefly noted in **Part I**, the external temperature gradient does not strongly affect changes in stress and strain within the inclusion. **Fig. 3** shows the result of steady state solution for a 1m spherical temperature drawdown (ΔT=-200°C) with large external thermal gradient (**A**) and small external thermal gradient (**B**). Both cases initially have a temperature of 220°C with an outer domain boundary (r_1) with the same temperature (220°C). Two concentric spherical shells with an internal temperature boundary to represent the thermal gradient: (i) outer core (r_2) with temperature 220°C and (ii) inner core (r_3) with temperature 20°C. In this case the steady state temperature solution can be divided into three layers: (i) interior shell ($r<r_1$) with uniform temperature 20°C, (ii) intermediate shell ($r_1<r<r_2$) with temperature gradually changing from 20°C to 220°C and (iii) area beyond outer boundary ($r_2<r$) with uniform temperature T=220°C. In **Fig 3**, **case A** represents a larger thermal gradient r_2=20m and **case B** represents a small thermal gradient r_2=1.5.

Fig. 3 A-1 and **B-1** shows the resulting strain response for the two cases. We use a volumetric thermal expansion coefficient $\alpha_v=3\times10^{-5}$ $E_{host}=E_{res}$ and Poisson's ratio v=0.2. With these parameters, Eqn (10) in part I (which is identical to the Eshelby solution since $E_{host}=E_{res}$) is able to evaluate volumetric strain as 3×10^{-3}. Both cases shows uniform volumetric strain within the inner core with a magnitude identical to the analytic solution $\varepsilon_v=3\times10^{-3}$ regardless of the size of the external thermal gradient. The result indicates that the external thermal gradient does not affect the stress/strain field inside the uniformly cooled reservoir. This implies that the stress, the strain and therefore the generated permeability change may be approximately estimated from the temperature change and the shape of cooled volume even without considering the external gradient. Thus, with these results, the complex response of thermally-induced permeability evolution can be approximated.

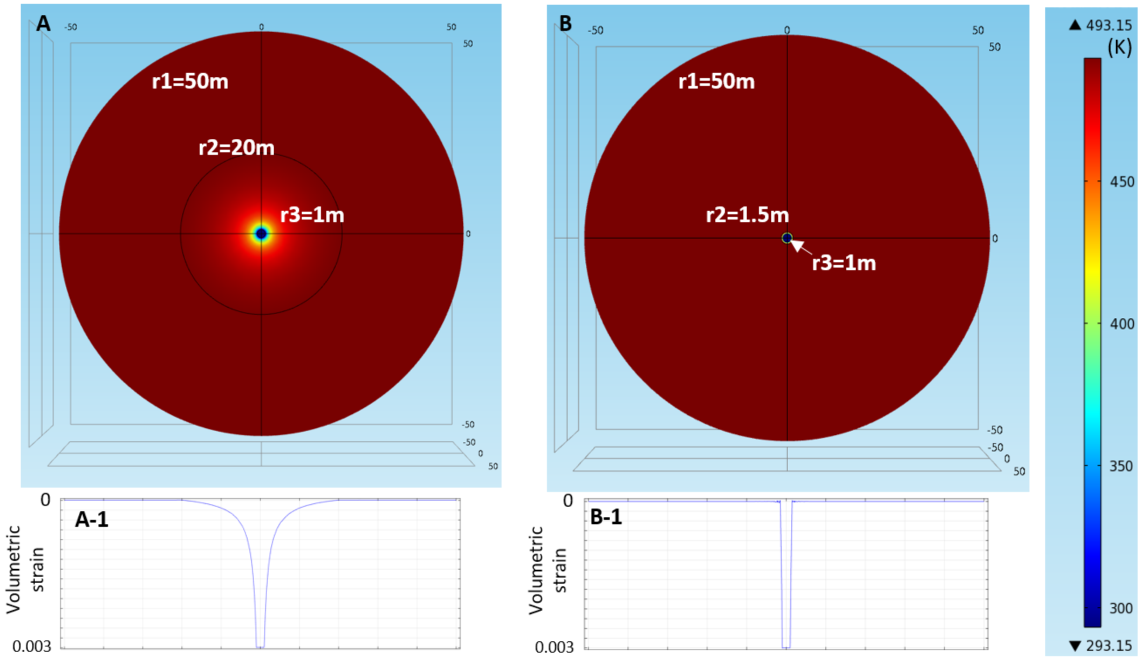

Figure 3. Steady state solution of temperature distribution with large thermal gradient (A) and small thermal gradient (B). A-1 and B-1 result in volumetric strain respectively to A and B.

2.2 Normal/Shear Deformation and Measurement with the HPP tool

Pressurization and thermal unloading results in the deformation of the reservoir. When the reservoir contains a discontinuity (fracture), both normal and shear deformations are expected on that feature. Gan and Elsworth (2014) investigated two modalities of fracture deformation - they are: (i) early time deformation induced by pressure and (ii) late time deformation induced by thermal unloading. **Part I** suggests a connection between surface deformation and thermal stressing in geothermal reservoirs. Thermal stress continues to evolve until the reservoir is fully depleted. However, pressure changes are typically concentrated during the early stages of injection and are typically localized to the near-wellbore region. These observation suggests that the permeability field initially evolves in response to changes in pressure and is then controlled by thermal stressing.

2.2.1 Simulation Method

We follow the thermo-hydro-mechanical (THM) response using the ToughtReact-FLAC3D coupled simulator (Taron and Elsworth, 2009) for a total period of 3×10^6 s (~35 days). The model geometry is illustrated in **Fig. 4** and the parameters used in the simulation are listed in **Table 1**. The domain represent ¼ of the cylindrical reservoir with a height 200m and radius 100 m. A wellbore is placed at the center with a radius of 10 cm. Isotropic normal stresses 35 MPa and a shear stresses of 10 MPa (x-z plane) are applied. Fixed displacement is applied on the outer reservoir boundaries and roller boundaries are applied on the inner reservoir boundary (z=0 and y=0). Initial fluid pressure is uniform 10 Mpa.

Two different properties are assigned in the reservoir to represent both: (i) matrix elements and (ii) fracture elements (**Fig. 4**). The matrix elements have high modulus (30 GPa) and are fully elastic (no failure). Conversely, the fracture elements have a low modulus (30 MPa) representing compliant response and fail with a tensional stress of 0.5MPa. These elements are represented by a Mohr-Coulomb criterion with a friction angle of 35° and with cohesion of 0.1 MPa. The fracture elements represent a thin fracture zone with a thickness of 4mm (2mm half aperture). Fluid flows almost exclusively into the fracture element due to an extremely small permeability (1 nano-Darcy) of the matrix elements. In this model, to focus on observing the thermal effect and to implement a uniform flow rate, a constant permeability is assigned without coupling with aperture. Therefore once the pressure field becomes steady state in the initial stage, the pressure in the fracture reaches a steady state. We test two cases of injection pressures (15 MPa and 30 MPa) to analyze the response from two different combinations of flow rate and thermal conductivity.

Property	**Value**	**Property**	**Value**
Reservoir Temp.	200ºC	Matrix Permeability	1 nano-Darcy
Injection Temp.	30ºC	Fracture Permeability	10 Darcy
Rock Density	2480 kg/m^3	Matrix Bulk Mod.	30 GPa
Specific Heat of Rock	1200 J/kg	Fracture Bulk Mod.	30 MPa
Heat Conductivity	3000 /K	Initial Pressure	10 MPa
Volumetric Therm. Exp.	3×10^{-5} /K	Injection Pressure	15/30 MPa
Normal Stress	35 Mpa isotropic	Friction Angle	35°
Shear Stress x-z	10 MPa	Cohesion	0.1 MPa

Table 1. Input parameters for the simulation. Fluid properties are calculated in ToughReact EOS.

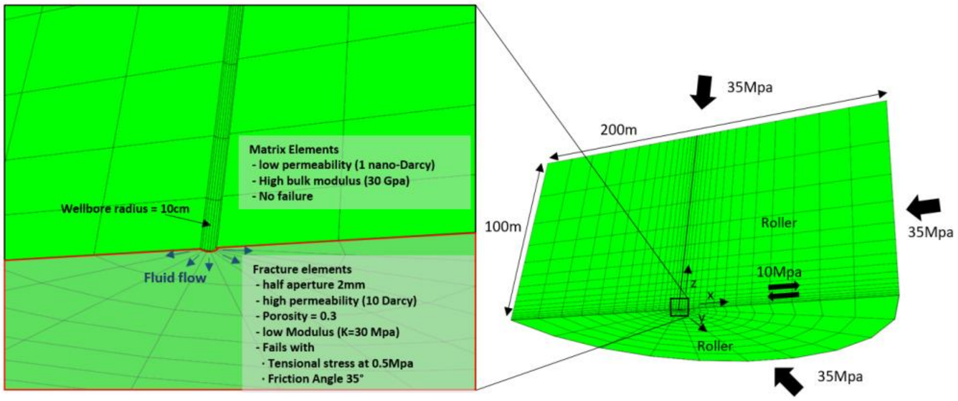

Figure 4. Model geometry. Simulated reservoir is ¼ of cylindrical reservoir with 200 m height and 100 m radius.

2.2.2 Simulation Results

Fig. 5 shows the displacement of the fracture wall resulting from the injection of cold water into a fracture that reaches to 30m from the wellbore (see box in **A-1**). Shown are displacements of one side of fracture - total offset is double. The results illustrate that the initial opening is due to pressurization and that late time response is due to thermal opening and slip. Initial normal opening, due to pressurization, is ~0.08 mm at 15 MPa and ~0.34 mm with 30 MPa injection pressure. The magnitudes are near-proportional to over-pressures from the initial pressure (5 MPa and 20 MPa), showing that the dilation is an elastic response modulated through the fracture compliance. The pressure response at the very beginning of the injection stage (~10 s) represents steady state and is static.

The thermal response of both normal and shear deformations are significant and detectable after 10^4 seconds (~2 h). Both cases show a maximum normal displacement of ~1.5 mm (total ~ 3mm) and a shear displacement of ~3 mm (total ~6 mm) after about one month of injection. Unlike the normal displacement profile, the shear displacements are not symmetric with the peaks shifted slightly to the left due to thermal contraction and resulting lateral translation of the medium.

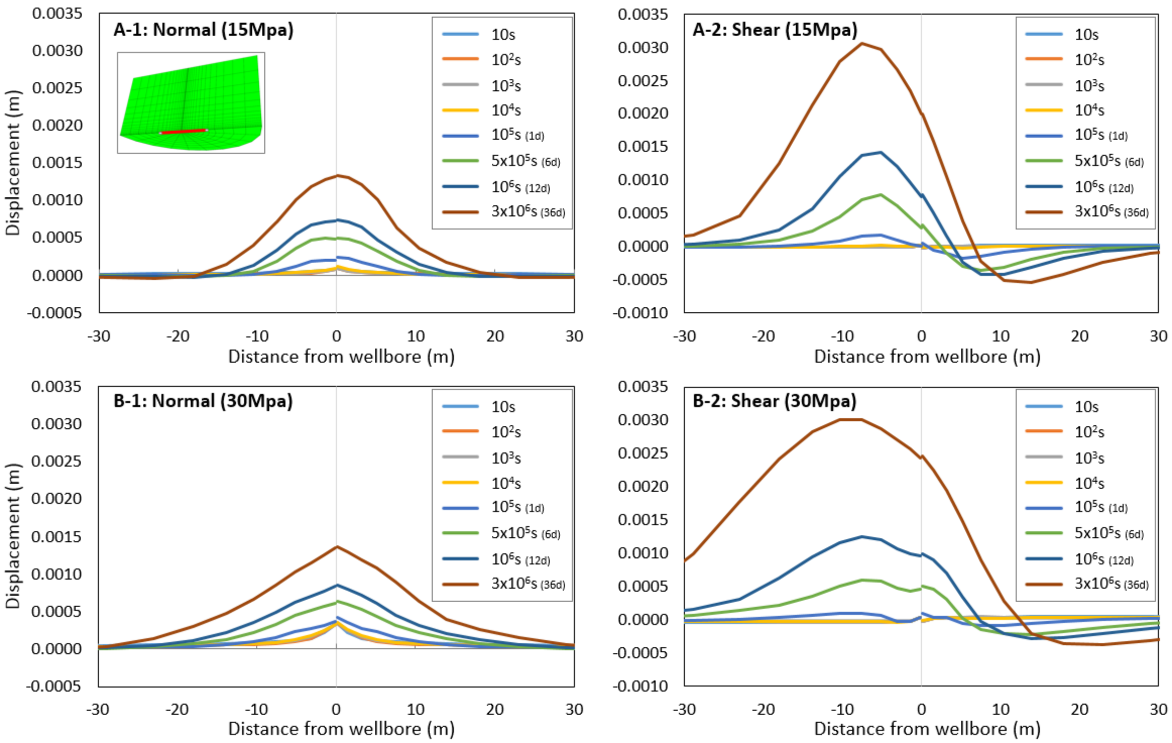

Figure 5. Normal and shear displacements near (30 m radius) the wellbore. A-1 and A-2 show normal and shear displacement induced with an injection pressure of 15 MPa and B-1 and B-2 show normal and shear displacement induced with an injection pressure of 30 MPa. The inset in A-1 illustrates the location of the plotted deformations within the reservoir.

Although in the 30 MPa case the injected volume is ~4 times larger, the maximum magnitude of the temperature induced displacements are similar in both high pressure and low pressure cases.

This result represents the control of the cooling shape on the evolution of the stress field. **Fig. 6** shows the temperature distribution within a radius of 30 m of the wellbore after both 1 day and 36 days and subject to each injection pressure. The distribution clearly shows that the total cooled area is larger for the 30 MPa injection pressure and the resultant shape of the cooled zone is also much flatter than that for the 15 MPa injection. The Eshelby solution (**Fig. 1-C)** indicates that the magnitude of the normal unloading for the flat ellipsoid (low *b/a*) is smaller than that for spherical cooling. For example, if the cooled shape is absolutely flat (*b/a~0*) then the reduction in the fracture normal stress becomes negligible. Note that the driving mechanism of both normal and shear deformations in this simulation is the cooling-induced reduction of the fault normal stress. Therefore, even with an injection volume 4 times larger, the maximum displacement responses are similar. However, the radius of the deformed area is larger for the larger injection volume.

The temperature distribution shows that the shape of the cooled zone is flat in both cases. This implies that there will be a significant reduction in the horizontal stress. In the simulations, the horizontal stresses in both cases evolve to approximately +50 Mpa (tension) around the wellbore. Although the matrix elements in this simulation are not allowed to fail, such a magnitude of tensional stress should generate thermal cracking (**Fig 2**) – vertical fractures normal to the mail horizontal fractures would result in increased vertical permeability. In addition, the evolution of the temperature distribution indicates that the aspect ratio *b/a* of the cooled spheroid increases with time. This implies short-term thermal cracking will initially develop on the fracture and normal opening will become significant as cooling progresses.

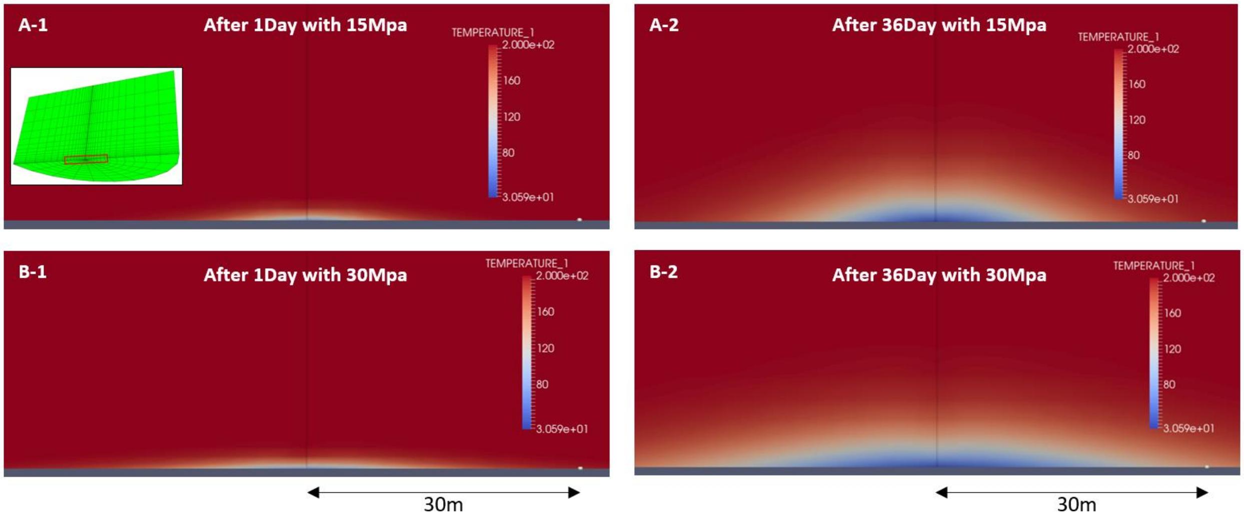

Figure 6. Temperature distribution after 1 and 36 days of injection at A: 15 MPa and B: 30 MPa injection pressure.

Fig. 7 illustrates the time dependent displacement of the HPP probe at the anchors and at the fracture wall during the 36 days of the simulation. The position where the displacements are measured in the model is illustrated in **Fig. 7 C**. Since the HPP measurements are based on the relative displacement between the anchors set both above and below the fracture, the HPP tool response can be represented as a displacements measured 0.3 m offset (above and below) from the fracture wall. The solid line denotes the normal displacement, the dashed line the shear displacement, blue line the fracture wall displacement and the orange line the anchor displacement. Note that all displacements represent only the upper reservoir. Therefore total opening and shear displacements should be these magnitudes, doubled.

Observed magnitudes of all displacements are significantly greater than the HPP resolution. Opening and shear displacements are larger than 1 mm at the fracture wall. Initial pressure-induced fracture dilations are ~0.08 mm and ~0.34 mm which are significantly larger than the tool resolution of ~1μm. Thermally induced shear and normal displacements reach the scale of several mm. The tool response of the shear displacements behave similarly to the displacement of the fracture wall. However normal displacements shows significantly different responses between the HPP response and that at the fracture wall. At ~10^3~10^4 s the two behaviors decouple as the displacements at the fracture wall begin to increase (fracture opening) while the HPP response begins to decrease. This HPP response reflects thermal contraction in the system. This is despite the fracture dilating. The overall displacement of the anchor is in the opposite sense to that of the fracture wall due to thermal contraction of the reservoir between the anchor and the fracture. After sufficient time (2~3×10^5 s), when the thermal front reaches the position of the HPP anchor, the response of tool and fracture are synchronous. This observation identifies that the HPP tool response represents the aggregate *in situ* thermal properties of both rock (thermal expansion coefficient and thermal conductivity) and fracture (stiffness, stress state and shear dilation). Thus the tool signal must be deconvolved to define the response of the fracture, in isolation – as this will define the permeability evolution of the fracture – the key measurement defining behavior of the system.

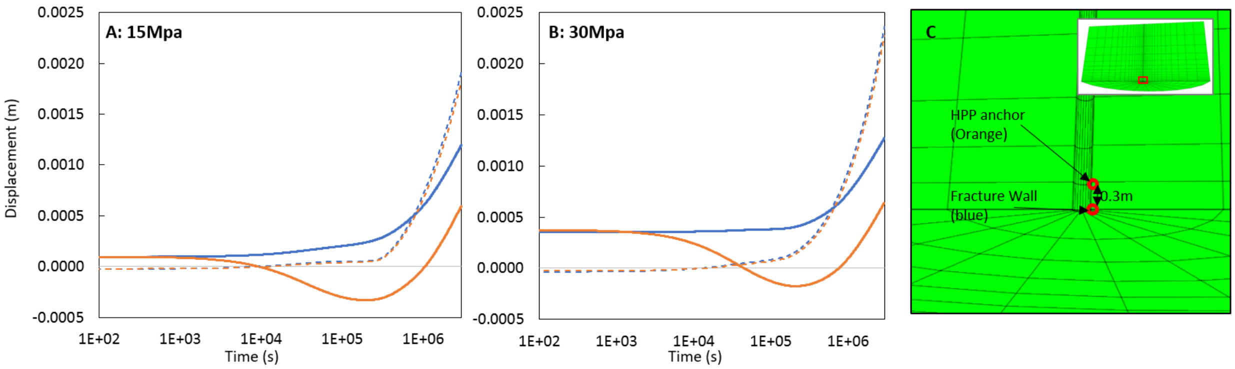

Figure 7. Wellbore response of fracture wall and HPP anchor. Each response is denoted as blue: fracture wall, orange: HPP tool response, solid line: fault opening displacement and dashed line: fault shear displacement.

3. Engineering Design of the Hot-HPP Tool

The current Cold-HPP-Tool is a unique packer system that allows a zone of a borehole to be hydraulically isolated by packers to allow standard fluid injection tests. A unique feature of the instrument is that it precisely measures deformations that occur as a result of the fluid injection and therefore enables the deconvolution of complex THMC effects that are key in defining the evolution of geothermal reservoirs. These deformations are measured both along the axis of the borehole and across the borehole allowing the full deformation tensor to be determined. Thus, this allows active injection and fault reactivation experiments to be conducted while fluid pressures are maintained and flow rates measured. As such, the tool allows both *in situ* characterization of hydro-mechanical properties at appropriate (field) scales and under *in situ* conditions, but also potentially allows resolution of the stress regime. In addition, this allows frictional characteristics to be determined along fractures by conducting miniature fracture slip experiments (e.g. Gugliemi et al., 2015 a&b). These data are crucial in constraining models for coupling stress to permeability and in defining important characteristics related to induced seismicity. The Cold-HPP has been extensively validated in these modes (e.g. Gugliemi et al., 2015 a&b).

3.1. Existing Cold HPP Tool Prototype and Principal Refinements

The existing Cold-HPP-Tool prototype has been qualified in 20-to-50m deep open boreholes in fractured shales and in carbonates, showing that sub-micron-scale displacements may indeed be captured with high resolution on fractures stimulated at injection pressures up to 6 MPa and temperatures to 20°C.

The Cold-HPP-Tool comprises a double-packer assembly separated by a 1-to-2.4 m long straddle with a displacement-measuring cage placed at mid-separation between the packers (**Fig. 8**). The cage is a 0.5 m long and 0.1 m diameter cylindrical element. At its upper and lower extent, the cage is attached to two rings that can be anchored to the borehole wall and straddle a fracture. Thus the cage is decoupled from the remaining straddle element and may record the deformation of the borehole on either side of a fracture transecting the borehole (**Fig. 8**). The key idea is that the cage is designed to deform in a way that captures the three-components of the displacement of the fractured borehole wall. All deformations and pressures are measured via fiber Bragg gratings and as such are substantially immune to temperature effects. Crucially, the DAQ and interrogation equipment is up-hole and remote from potentially high down-hole temperatures.

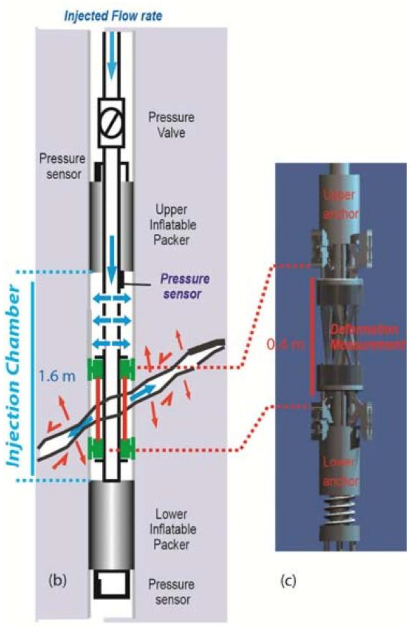

Figure 8. The HPP tool (center) comprises an upper and lower packer (grey) that isolates a zone allowing the forced injection of water (blue arrows) under pressure. A deformation cage (green) is clamped to the borehole wall and measures relative deformations axial-to and across (shear) the borehole. This central zone precisely measures relative displacements in shear and in dilation and is the essential component of the instrument shown on the tool itself (right).

Key design upgrades to push towards an Hot-HPP-Tool include (i) exchanging latex packers to different packer technology (150°C-to-300°C and 30 to 100 MPa), (ii) refining the displacement-measuring cage to allow deployment in deep boreholes (100 MPa), (iii) ensuring measurement of pressures and displacement-cage strains at high temperatures (150°C to 300°C) and (iv) deploying and recovering the tool *via* an armored umbilical or by coiled tubing (3 km).

The Cold-HPP-Tool consists of a packer, an anchor and a deformation-measuring unit. Since the tool measures the relative displacement between anchors that straddle a central fracture, the anchor must attach firmly to the borehole wall. Therefore the anchor-deformation unit is mechanically decoupled from packer-straddle so that the stiffness of the straddle coupling will not apply extra load on the anchor grip. A simplified design for this system would be to use the packer to perform both zonal-isolation and cage-anchoring functions and to then calibrate-out the strain that may be induced by the pressurization of injection chamber. This would incorporate the cage-anchoring task into packer deployment/recovery, thus eliminating one task and an additional hydraulic line (the anchors in the Cold-HPP-Tool are hydraulically deployed) and simplifying overall operation of the probe.

To further upgrade the Cold-HPP-Tool to survive at 100 MPa/150°C to 300°C, several challenging problems need to be solved. Fortunately, the fiber Bragg gratings (FBGs) that measure straining of the displacement cage, are stable at high pressure and high temperature. However, the adhesives that are currently used to fix the strain gauges to the deforming cage are not durable to temperatures >110°C. The interrogation of these FBGs are by an up-hole/surface tool. Similarly, the main functions of the HPP-Tool (anchoring, deploying packers and measuring strains) are not electrically actuated. However, the current packer and anchor would not survive in an HPHT environment and must be replaced by suitable materials.

Alternatively, the use of downhole refrigeration may also be considered. Dewar-based subsurface cooling systems (with cryogenics) have been successfully deployed to protect delicate image-logging tools (Massiot et al, 2015). Refrigeration provides the option to deploy delicate electronic devices or electric pumps (for subsurface control) downhole – and could allow the existing Cold-HPP with its complex controls to be deployed with only minor modification. However, the deployment will necessarily be for limited duration and this will significantly increase the complexity of tool (feasible deployment for 10 hours at 275°C, Massiot, 2015). Conversely, in the absence of refrigeration, making the tool simpler and more robust will require a significant modification in the design, but ultimately will simplify repeated deployments and operation.

The following identifies key design considerations in transforming the Cold-HPP-Tool (6 MPa/70°C) into one capable of operating to 100 MPa/>150°C-to-<300°C - the Hot-HPP-Tool.

3.2 Selection of Packers for Integration in the HPP-Tool

A durable packer assembly that substitutes for temperature-vulnerable elastomers is a primary need for the hot tool. The essential functions of a packer required for Hot-HPP operation are (i) high temperature (~300°C) durability for several hours (ii) high maximum differential pressure and (iii) retrievability. In addition a high inflation grip and high relative stiffness are highly desirable functions so that the packer can also serve as an anchor. Combining the packer and displacement-cage would both simplify the tool and make it more robust.

There are several commercial packers that survive to temperatures of >300°C. Those commercial packers, however, are not readily applicable to the current Cold-HPP-Tool design due to difference in operation. The Cold-HPP uses Bimbar-type packers that inflate/deflate with fluid pressurization/depressurization via a pressurized tubing connection – typically actuated from the surface/borehole-collar. Conversely, commercial high temperature packers operate by dropping a ball along a coiled-tube umbilical with this ball seating into a collared-constriction at the packer base. Subsequent pressurization of the umbilical then inflates the packer (**Fig 9**), the ball acting as a recoverable plug. This ball-drop technique is well-proven and widely-used in the subsurface service industry and could be used to both improve the robustness and operational reliability of the packer/cage assembly. However, adopting his technique will necessitate a complete redesign of deformation-measuring cage if affixed to the packer – as proposed. Although not common, off-the-shelf high pressure and retrievable packers offer a straightforward solution.

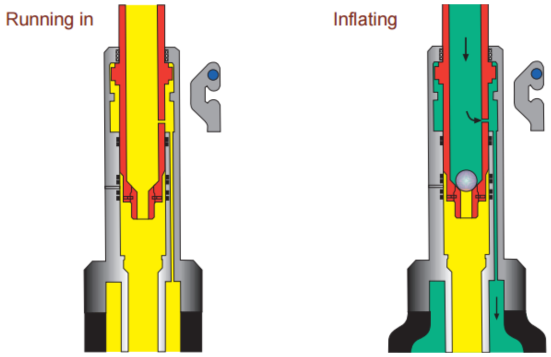

Figure. 9. Ball-drop packer inflation system. Packer in red. Pressurized stream (right) in green. (figure from Tam International).

Some HNBR (Hydrogenated nitrile) packers will operate to 150°C with a low expansion ratio, and packers with operational temperatures to 300°C are available from at least three suppliers with two of these being retrievable (Packer-Plus Inferno packers-315°C, Schlumberger MH Thermal packer-343°C). These packers would require to be tested at high temperature from >130°C to <300°C in the laboratory, to estimate the limiting conditions that satisfy both the anchoring and the sealing roles that packers must play during the HPP-Tool testing procedure.

3.3 Deformation-Measurement Cage Design

To meet the requirements for the Hot-HPP, a deformation cage should be re-designed to measure micrometer-to-millimeter displacements of a borehole wall interval pressurized up to 100 MPa with water temperatures to 300°C, and injection rates of 0.1< to ~40 L/Min. The main function of deformation cage (fiber Bragg gratings) is to survive in the required HPHT environment. However, different from the current cage on the Cold-HPP, it is desirable that the new cage is milled from a single solid metal cylinder – the exact composition guided by needs of durability and the design environment.

Additionally, although no significant modifications are anticipated to this system, testing different adhesives that maintain the strain gauge coupling to the deforming cage at high temperature and high water pressure is required.

4. Conclusions

We explore mechanisms of deformation induced by the injection of cold water into a single fracture and the expected signals that may be recovered from the HPP tool. The impacts of thermal stress are evaluated as an Eshelby inclusion. These results indicate that the induced stress fields are strongly dependent on the shape of the cooling envelope. When cooling is of the form of a flat spheroid encasing the horizontal fracture, thermal unloading is a minimum in the vertical direction. This minimizes the aperture increase while the unloading is maximum in horizontal direction (fracture parallel) and may generate vertical thermal cracking normal to the horizontal fracture. Conversely, as the spheroid becomes progressively equi-axial, the, magnitude of the vertical unloading becomes significant, opens the main fracture and may eventually generate normal (tensional) opening. This result indicates that the evolution of the stress field and permeability in an EGS reservoir will be strongly dependent on not only the thermal expansion coefficient and change in temperature but also shape of cooling that is dependent on fluid flow rate, thermal conductivity and duration of cooling.

Thermally-induced deformation is further analyzed with numerical simulations using two different injection pressures. Simulation results illustrate an initial immediate opening due to the pressurization of a compliant fracture and following slow but continuous thermally-induced opening and shear deformation. Anticipated HPP signals (deformations measured at the anchor points at 30 cm above and below the fracture) are significantly larger than tool resolution confirming the utility of the tool to precisely measure reservoir hydro-thermal-mechanical properties and to describe reservoir deformation behavior. The normal displacement signal recorded from the HPP tool will initially be one of compaction (until $2\sim3\times10^5$ s) reflecting the thermal contraction of the reservoir rock rather than the behavior of the fracture. This signal will then change to one of dilation reflecting the true fault normal opening response. The phantom compactive response must be corrected to determine the fracture response, or reduced by migrating the tool anchor points closer to the fracture. Conversely, the shear deformation signal always directly replicates fault wall shear deformation. These normal and shear deformation and signal behaviors are strongly dependent on the combination of flow rate, thermal conductivity, thermal expansion coefficient and test duration. Calibrating HPP tool response with permeability evolution will provide essential parameters to define the evolution of geothermal reservoirs.

Current HPP tool capabilities and necessary upgrades for deployment in geothermal systems as the Hot-HPP tool are also evaluated. The fiber Bragg gratings (FBGs), that measure strain in the displacement cage, are stable at high pressure and high temperature since the interrogating device is retained outside the hot zone. However the packer and deformation cage of the current tool will need to be replaced or redesigned. We review several off-the-shelf HTHP packer options. Although several functions such as test duration or retrievability need to be further evaluated, a number of commercial HTHP packers exist that meet the design requirements. For the deformation cage, a different alloy and cage-fiber adhesive combination are required. Although the cage itself may not require significant modification or redesign, except for the substitution of materials, adopting an off-the-shelf packer may require the entire tool to be re-designed to comply with the operation and control system of a commercial packer system.

Acknowledgements

This work is a partial result of support provided by DOE Grant DE-EE0006761. This support is gratefully acknowledged.

References

Cappa F., Guglielmi Y., and Virieux J., 2007. Stress and fluid transfer in a fault zone due to overpressures in the seismogenic crust. Geophys Res Lett, 34, L05301, doi:10.1029/2006GL028980.

Candela, T., Brodsky, E.E., Marone, C., and Elsworth, D. (2015), Flow rate dictates permeability enhancement during fluid pressure oscillations in laboratory experiments, J. Geophys. Res. Solid Earth, 120.

Candela, T., Brodsky, E., Marone, C., Elsworth, D. (2014) Laboratory evidence for particle mobilization as a mechanism for permeability enhancement via dynamic stressing. Earth and Plan. Sci. Lett. Vol. 392. pp. 279-291.

Derode B., Guglielmi Y., De Barros L., Cappa F. (2015). Seismic responses to fluid pressure perturbations in a slipping fault: Fault reactivation by fluid pressures. Geophysical Research Letters. 04/2015; DOI: 10.1002/2015GL063671.

Derode B., Cappa F., Guglielmi Y. and Rutqvist J. (2013). Coupled seismo-hydromechanical monitoring of inelastic effects on injection-induced fracture permeability. International Journal of Rock Mechanics and Mining Sciences 61, 266-274.

Elsworth, D., (2001), Mechanical response of lined and unlined heated drifts: Rock Mechanics and Rock Engineering, v. 34, p. 201–215, doi: 10.1007/s006030170009.

Elsworth, D., Mattioli, G., Taron, J., Voight, B., and Herd, R., 2008, Implications of magma transfer between multiple reservoirs on eruption cycling: Science, v. 322, p. 246–248.

Eshelby, J.., 1957, The determination of the elastic field of an ellipsoidal inclusion, and realted problems: Proceedings of the Royal Society,.

Gan, Q., and Elsworth, D., (2014), Analysis of fluid injection-induced fault reactivation and seismic slip in geothermal reservoirs.: Journal of Geophysical Research : Solid Earth, p. 3340–3353, doi: 10.1002/2013JB010679.Received.

Guglielmi Y., Cappa F., Avouac J.P., Henry P., Elsworth D. (2015a). Seismicity triggered by fluid-injection-induced aseismic slip. Science 12 June 2015, Vol. 348, Issue 6240.

Guglielmi Y., Elsworth D., Cappa F., Henry P., Gout C., Dick P., and Durand J. (2015b). In Situ observations on the coupling between hydraulic diffusivity and displacements during fault reactivation in shales. Journal of Geophysical Research: Solid Earth, 120, doi: 10.10002/2015JB012158

Guglielmi Y., Henry P., Cappa F. and Derode B. (2013a). Relationships between slow slip, seismicity and fluids leakage during a pressurized fault zone rupture in situ experiment:

Importance for reservoir/caprock stimulation monitoring and efficiency assessment. ARMA 13-517, San Francisco 2013.

Guglielmi Y., Cappa F., Lançon H., Janowczyk, Rutqvist J., Tsang C.F. and Wang J.S.Y. (2013b). ISRM Suggested Method for Step-Rate Injection Method for Fracture In-Situ Properties (SIMFIP): Using a 3-Components Borehole Deformation Sensor. Rock Mechanics and Rock Engineering, DOI 10.1007/s00603-013-0517-1.

Guglielmi Y., Cappa F., Amitrano D., (2008). High-definition analysis of fluid-induced seismicity related to the mesoscale hydromechanical properties of a fault zone. Geophys Res Lett, Vol.35, L06306, doi:10.1029/2007GL033087.

Im, K., Elsworth, D., Guglielmi, Y., and Mattioli, G.S., (2016), Geodetic imaging of production, thermal depletion and fault reactivation in geothermal reservoirs: Submitted,.

Jeanne P., Guglielmi Y., Cappa F., Rinaldi A. and Rutqvist J. (2014). Effects of lateral permeability evolution on faults zones reactivation by industrial fluid pressurization in deep reservoir: Application to CO2 sequestration problems. Journal of Structural Geology, Volume 62, May 2014, pages 97-108.

Jeanne P., Guglielmi Y. and Cappa F. (2013). Hydromechanical heterogeneities of a mature fault zone: impacts on fluid flow. Groundwater, doi: 10.1111/gwat.12017.

Liu, J., Elsworth, D., Brady, B.H., and Muhlhaus, H.B., 2000, Strain-dependent Fluid Flow Defined Through Rock Mass Classification Schemes: Rock Mechanics and Rock Engineering, v. 33, p. 75–92.

Murdoch, L.C., Germanovich, L.N., Wang, H., Onstott, T.C., Elsworth, D., Stetler, L., Boutt, D. (2012) Hydrogeology in the vicinity of Homestake mine, South, Dakota, USA. J. Hydrol. Vol. 20, Vol. 1. pp. 27-43. http://dx.doi.org/10.1007/s10040-011-0773-7.

Okada, 1985, Surface deformation due to shear and tensile faults in a half-space: International Journal of Rock Mechanics and Mining Sciences Geomechanics Abstracts, v. 75, p. 1135–1154, doi: 10.1016/0148-9062(86)90674-1.

Polak, A., Elsworth, D., Yasuhara, H., Grader, A.S., and Halleck, P.M. (2003) Permeability reduction of a natural fracture under net dissolution by hydrothermal fluids, Geophys. Res. Lett., 30(20), 2020.

Taron, J., and Elsworth, D., 2009, Thermal-hydrologic-mechanical-chemical processes in the evolution of engineered geothermal reservoirs: International Journal of Rock Mechanics and Mining Sciences, v. 46, p. 855–864, doi: 10.1016/j.ijrmms.2009.01.007.

Segall, P., and Fitzgerald, S.D., 1998, A note on induced stress changes in hydrocarbon and geothermal reservoirs: Tectonophysics, v. 289, p. 117–128, doi: 10.1016/S0040-1951(97)00311-9.